UNIVERSIDADE
EDUARDO
MONDLANE

ESCOLA SUPERIOR DE CIÊNCIAS MARINHAS E COSTEIRAS

Master's Dissertation in Applied Oceanography

Dynamics of the Mozambique Channel using surface drifters and satellite-derived geostrophic and Ekman currents

Nélio das Neves Olívio Sitoe

Quelimane

February 2025

UNIVERSIDADE
EDUARDO
MONDLANE

ESCOLA SUPERIOR DE CIÊNCIAS MARINHAS E COSTEIRAS

Dissertation submitted as a partial requirement for obtaining the Master's degree in Applied Oceanography

Dynamics of the Mozambique Channel using surface drifters and satellite-derived geostrophic and Ekman currents

Author

Nélio das Neves Olívio SITOE

Doutora Maria Helena Paulo ANTÓNIO, Jury president

(Universidade Eduardo Mondlane, Mozambique)

Professor Doutor Tor GAMMELSRØD, Supervisor

(University of Bergen, Norway)

Doutor Avelino Ângelo Adolfo LANGA, Supervisor

(Universidade Eduardo Mondlane, Mozambique)

Doutor Issufo HALO, Examiner

(Department of Forestry, Fisheries and the Environment, South Africa)

Quelimane

February 2025

Dedico este trabalho aos meus Pais.

Acknowledgements

I express my sincere gratitude to Professors Tor Gammelsrød, Avelino Ângelo Adolfo Langa and António Mubango Hoguane for their guidance, support and criticism while writing this thesis. Your experience and dedication were essential for this work. I deeply thank my parents and siblings for their constant love and support, as well as my friends for their motivation and company in challenging moments. To my co-workers, thank you for your understanding and helping to make this journey lighter. Each of you contributed partially to this realisation, which was only possible thanks to your support and encouragement.

Thank you.

Declaration of honour

I, **Nélio das Neves Olívio Sitoe**, declare that this dissertation was never presented to obtain any academic degree and constitutes the result of my work. This dissertation partially complies with the requirements for obtaining the Master's degree in Applied Oceanography from Eduardo Mondlane University.

(Nélio das Neves Olívio Sitoe)

Date: February 2025

Resumo

Este estudo examinou a dinâmica das correntes superficiais em torno de Madagascar e do Canal de Moçambique. A divisão dessas regiões em sub-regiões do Este da costa de Madagascar, Norte, Centro e Sul do Canal de Moçambique permitiu a avaliação do papel das correntes geostróficas e a combinação entre correntes geostróficas e de Ekman na dinâmica sub-regional. No entanto, bóias de deriva virtuais foram comparadas com 151 bóias de deriva SVP com resolução temporal de 1 hora do *Global Drifter Program*, durante 2000 à 2019. Adicionalmente, enquanto algumas bóias de deriva SVP mantiveram suas velas de deriva, outras as perderam; essa característica foi considerada na análise. As trajetórias das bóias virtuais foram calculadas usando a equação básica de modelação Lagrangiana, que requer campos de velocidade. Estes campos são baseados no modelo de topografia dinâmica média dos oceanos CNES-CLS18, que compreende observações de altímetro de satélite, vento de modelos numéricos e observações in-situ de bóias SVP. Em complemento, estes são compilados em quatro níveis de processamento pelo Serviço Marítimo da União Europeia-Copernicus. As bóias de deriva virtuais calculadas apartir dos dois campos de velocidade foram designados como *Virtual Geostrophic Drifter* (VGD) e *Virtual Geostrophic-Ekman Drifter* (VGED), enquanto as bóias de deriva SVP foram classificadas como bóias reais. Os resultados revelam subestimações substanciais, com uma média de 29% com VGDs e melhorando para 21% quando o desvio de Ekman é incorporado nos VGEDs em comparação com as bóias reais. Este facto mostra melhoria no modelo de topografia dinâmica média dos oceanos CNES-CLS18. A costa Este de Madagascar exibiu as maiores discrepâncias de velocidade devido ao dipolo formado na ponta sul de Madagascar, o que impediu o movimento de VGD específico para o canal. Ao mesmo tempo, o Norte do Canal de Moçambique mostrou menor subestimação devido às fortes correntes de fronteira ocidental, ventos locais e ciclones tropicais, destacando o domínio da sazonalidade do vento na sub-região. Devido ao comportamento linear e não linear dos vórtices, as bóias virtuais apresentam erros de posição substanciais no Canal Central e Sul de Moçambique em relação às bóias reais. Entretanto, as bóias virtuais não conseguiram identificar as principais estruturas submesoescala porque a resolução de 25 km dos campos de velocidade foi um problema significativo. A dispersão de bóias virtuais próximo a costa de Cabo Delgado foi influenciada por correntes sazonais da deriva superficial de Ekman. Isso destaca a necessidade de incorporar essas dinâmicas em simulações futuras à medida que os ventos modulam essa região. Uma parte considerável dessas bóias virtuais encalharam logo após serem liberadas devido aos fortes ventos do sul que influenciam a superfície do oceano, deslocando-as para a costa Este de África. Esse fenômeno foi observado predominantemente no inverno.

Palavras-chave: Dispersão de particulas, Canal de Moçambique, Bóias de deriva de superfície, Correntes geostróficas, deriva de Ekman

Abstract

This study examined the surface current dynamics around Madagascar and the Mozambique Channel. Dividing these regions into the Eastern Madagascar Coast, Northern, Central, and Southern Mozambique Channel subregions allowed for the assessment of the role of geostrophic-only and combined geostrophic and Ekman currents in the dynamics. Moreover, calculated virtual drifters were compared with 151 hourly Surface Velocity Program drifters (SVP drifters) from the Global Drifter Program spanning from 2000 to 2019. In addition, while some SVP drifters retained their drogues, others lost them; this status was considered in the analysis. The virtual drifter's trajectories were calculated using the basic Lagrangian modelling equation, which requires velocity fields. The velocity fields employed are based on the CNES-CLS18 mean dynamic topography model, which comprises satellite altimeter observations, wind from numerical models and in-situ observations from SVP drifters. These velocity fields are compiled at four levels of processing by the European Union-Copernicus Marine Service. The virtual drifters from the two velocity fields were designated as Virtual Geostrophic Drifter (VGD) and Virtual Geostrophic-Ekman Drifter (VGED), while the SVP drifters were classified as real drifters. The results reveal substantial underestimations, averaging 29% with VGDs and improving to 21% when Ekman drift is incorporated in the VGEDs compared to real drifters. This shows improvement in the CNES-CLS18 mean dynamic topography model. The Eastern Madagascar Coast exhibited the highest velocity discrepancies due to the formed dipole in the southern tip of Madagascar, which prevented the movement of specific VGD to the channel. However, the Northern Mozambique Channel showed lower underestimation due to strong western boundary currents, local winds, and tropical cyclones, highlighting the region's dominance of wind seasonality. Due to the eddy's linearity and non-linearity, virtual drifters have substantial position errors in the Central and Southern Mozambique Channel. Moreover, virtual drifters failed to identify key submesoscale structures because the velocity field's 25 km resolution was a significant issue. The dispersion of virtual drifters in the offshore Cabo Delgado coast of the Northern Mozambique Channel was predominantly influenced by seasonal Ekman-driven currents. This highlights the necessity of incorporating these dynamics into future simulations as winds modulate this region. A considerable part of these virtual drifters ran aground shortly after being released due to the strong winds from the south that influence the ocean surface, displacing them 45° to the left in relation to the wind's direction. This phenomenon was observed predominantly in winter.

Keywords: Particle tracking, Mozambique Channel, SVP drifters, Geostrophic currents, Ekman drift

Contents

Acknowledgements i

Declaration of honour ii

Resumo iii

Abstract iv

1 INTRODUCTION 1

1.1 Research problem . . . 3

1.2 Research objectives . . . 4

2 LITERATURE REVIEW 5

2.1 Mozambique Channel Circulation . . . 5

2.1.1 Atmosferic mechanism . . . 5

2.1.2 Mesoscale eddies . . . 7

2.2 Geostrophic and Ekman flow . . . 8

2.2.1 Geostrophic currents . . . 8

2.2.2 Ekman transport . . . 9

2.3 Global Drifter Programme . . . 11

2.3.1 Drifters dataset . . . 11

3 DATA AND METHODOLOGY 14

3.1 Area of study . . . 14

3.2 Surface drifter observations . . . 16

3.3 Velocity fields . . . 18

3.4 Particle tracking model . . . 20

3.4.1 Particle tracking . . . 20

3.4.2 Velocity conversion . . . 21

4 RESULTS 24

4.1 Drifters interaction with moving eddy . . . 29

4.2 CNES-CLS18 performance . . . 33

4.3 Drifter dispersion released within an area in the Northern Offshore of Cabo Delgado . . . 34

5 DISCUSSION **35**
5.1 Drifter within a moving eddy 40
5.2 Velocity field performance 42
5.3 Drifter dispersion in Northern Offshore of Cabo Delgado 46

6 CONCLUSION **47**

Bibliography **49**

A Method Description **55**
A.1 Cartesian coordinates from geographical coordinates 55
A.2 Geographical coordinates from cartesian coordinates 56

B Global Drifter Program **57**

C Tropical Cyclones **58**

D Virtual drifter dispersion within offshore of Cabo Delgado **60**

List of Figures

2.1 Climatological monthly means of wind stress (vectors) and wind stress curl (shading) are shown for different seasons: austral summer (a, JAN), autumn (b, APR), winter (c, JUL), and spring (d, OCT). Negative (blue) and positive (red) wind stress curls indicate areas favourable for upwelling and downwelling, respectively. The data were sourced from the Scatterometer Climatology of Ocean Winds (SCOW), as described by Risien and Chelton (2008), with a global spatial grid resolution of 1/4° × 1/4°, estimated from 10 years (September 1999 to August 2009) using measurements from QuikSCAT. Figure from Vinayachandran et al. (2021). 6

2.2 Bathymetry around Madagascar and the Mozambique Channel, along with the main currents and flow features. Figure from Schouten et al. (2003). 7

2.3 Schematic view of two SVP drifter types shown to scale; most of the tether length has been excluded. The drogues are centred at a depth of 15 m. Figure from Lumpkin e Pazos (2007). 12

3.1 West Indian Ocean, where black box represents the area of study in sub-regions Eastern Madagascar Coast (EMC), Northern Mozambique Channel (NMC), Central Mozambique Channel (CMC) and Southern Mozambique Channel (SMC). The stars represent SVP drifter initial position. The grey transparent lines are SVP drifter tracks. Cabo Delgado is represented for the purpose of demonstrating the province where natural gas is explored offshore. Created with PyGMT (Tian et al., 2024). Adapted from Hart-Davis et al. (2018). 15

3.2 Annual distribution of SVP drifters between 2000 and 2019. The number of drifters each year is shown above the bars. 17

3.3 Spherical and cartesian coordinate system, where ϕ is the latitude angle, λ is the azimuthal angle or longitude, and r is the distance from the origin at the centre of the Earth. Adapted from (Constantin & Johnson, 2018). 21

4.1 Trajectories of real drifter 40551 and two virtual drifters forced by geostrophic-only and geostrophic + Ekman currents. The real drifter (black) travelled for 77 days with a detached drogue, starting on 27 February 2008 and ending on 14 May 2008. The virtual drifters (VGD - red and VGED - blue) started from the same initial position, following a path for 77 days. The detachment of the drogue occurred prior to entering the domain. 24

4.2 Trajectories of real drifter 46070 and virtual drifters (VGD - red and VGED - blue) over 35 days. The real drifter travelled from 16 October 2009 to 20 November 2009 with a detached drogue before entering the domain. 25

4.3 Trajectories of real drifter *ID: 62575* and virtual drifters over a 43-day period. The real drifter travelled from 20 December 2009 to 1 February 2010 with a detached drogue. . . 26
4.4 Trajectories of real drifter (ID: 17442) and two virtual drifters over 35 days. The real drifter travelled from 28 March 2000 to 2 May 2000 with the drogue attached, following subsurface currents. 27
4.5 Trajectories of the real and virtual drifter (ID: 17442) across distinct stages. (a) and (b) panels show the progression of the drifter over time, with key differences in loop size and displacement highlighted by their mean diameters. The sea level L3 orbit from ERS-2 satellite, correspond to the period of 2000-03-29T07:38:29 to 2000-04-04T20:10:56 acquired from European Union-Copernicus Marine Service (2021). 29
4.6 Velocity time development of the real and virtual drifters (ID: 17442) across distinct stages. This represents the velocity during the progression in *Figure 4.5*; the solid lines are the velocity during the loops. 30
4.7 Trajectories of the real and virtual drifter (ID: 70972) across distinct stages. (a) and (b) panels show the progression of the drifter over time, with key differences in loop size and displacement highlighted by their mean diameters. The sea level L3 orbit from Jason-1 satellite corresponds to the period of 2010-10-04T16:00:00 to 2010-10-10T14:00:00 acquired from European Union-Copernicus Marine Service (2021). 31
4.8 Velocity time development of the real and virtual drifters (ID: 70972) across distinct stages. This represents the velocity during the progression in *Figure 4.7*; the solid lines are the velocity during the loops. 32
4.9 (a) Location of Area 4 in the Northern Offshore of Cabo Delgado. The stars represent the virtual drifter's initial positions determined randomly inside the Area 4 polygon. They were set to run for the entire month, with a time step of 1 hour. The geostrophic-only and geostrophic+Ekman velocity fields were used to calculate the trajectories. The overlap trajectories of these virtual drifters can be found in the Appendix D in *Figure D.1*. (b) Monthly mean distance travelled by 480 virtual drifters between 2000 and 2019. 34

5.1 Trajectories of the real and virtual drifter (ID: 62575) across distinct stages. (a) and (b) panels show the progression of the drifter over time. 37
5.2 Comparing velocity (left panel) and instantaneous displacement (right panel) distributions for real drifters and virtual drifters across four regions of the domain. IDs 40551, 46070, 62757, 17442 are within EMC, NMC, CMC and SMC regions, respectively. The boxes indicate the Interquartile Range (IQR), with a line inside each box showing the median value. Vertical bars, known as whiskers, extend to encompass the data range up to 1.5 times the IQR, while circles represent outliers that lie beyond this range. 38

5.3 Comparison of gridded $\frac{1}{8}^{\circ}$ mean velocities from 2000–2019, interpolated from all 151 real and virtual drifters. Blank areas represent regions without drifter data, where no velocity could be interpolated. 43

5.4 Frequency distribution of error distances (in km) between real and virtual drifter for the Virtual Geostrophic Drifter (VGD) and Virtual Geostrophic-Ekman Drifter (VGED) across four regions of the domain (A: Eastern Madagascar Coast, B: Northern Mozambique Channel, C: Central Mozambique Channel, D: Southern Mozambique Channel). Error distances are shown as percentage frequencies with a bin width of 12.5km, comparing the performance of VGD (red) and VGD (blue) in replicating drifter trajectories. The frequency percentage in these histograms represents the relative occurrence of each position error across the dataset of drifters. Each bar in the histogram indicates the percentage of total measurements that fall within a particular range of position error. 44

C.1 Track of Tropical Cyclone Hudah in the Southwest Indian Ocean, showing its progression from March 24, 2000, to April 9, 2000. The coloured dots represent different stages of intensity, following the standard classification system: CTTI (Cyclonic Tropical Storm), CTI (Intense Tropical Cyclone), CT (Tropical Cyclone), FTT (Moderate Tropical Storm), and TTM (Tropical Depression), with each stage depicted along the track based on meteorological data. Image from Météo France archives. 58

C.2 Track of Moderate Tropical Storm Bongani in the Southwest Indian Ocean, depicting its trajectory from November 20, 2009, to November 26, 2009. The cyclone moved north of Madagascar and gradually weakened. The coloured dots along the path indicate the cyclone's intensity stages: CTTI (Cyclonic Tropical Storm), CTI (Intense Tropical Cyclone), CT (Tropical Cyclone), FTT (Moderate Tropical Storm), TTM (Tropical Depression), and DT (Tropical Disturbance). Image from Météo France archives. 59

D.1 Trajectories of 480 virtual drifters, with half for VGD and half for VGED. These were released inside Area 4 (represented with magenta) of FLNG facility on the offshore coast of Cabo Delgado. The trajectories were calculated using the Geostrophic-only velocity field, represented in red, and the Geostrophic+Ekman velocity field, represented in blue. The figure represents an overlap of trajectories from 2000 to 2019. 60

List of Tables

2.1 Table of location, velocity, and temperature data products and availability from the GDP which defines three levels of data processing. Variables without asterisks are observations, while variables with asterisks are estimates. Only Level-3 data products are readily available from the GDP. Adapted from Elipot et al. (2022b). 13

3.1 Details SVP drifter passed through MC during 2000 to 2019 period. 17

3.2 Overview of the CMEMS datasets used for particle tracking. 18

4.1 Percentage of velocity underestimation for geostrophic and geostrophic plus Ekman currents compared to real drifters in different regions of the domain (refer to *Figure 3.1*). The integration time column represents the percentage of total time steps from the real drifter data covered by the virtual drifters. The integration time percentage reflects the extent to which the virtual drifters either ran aground or left the velocity field's domain. Inside brackets, there are a number of drifters by region and velocity fields. 33

B.1 GDP drifters characteristics IDs. 57

List of Acronyms and Glossary

AOML	NOAA's Atlantic Oceanographic and Meteorological Laboratory
CMC	Central Mozambique Channel
CMEMS	Copernicus Marine Environment Monitoring Service
ECMWF	European Centre for Medium-Range Weather Forecasts
EMC	Eastern Madagascar Coast
EOF	Empirical Orthogonal Function
ERA5	Fifth Generation ECMWF Atmospheric Reanalysis of the Global Climate
GDP	Global Drifter Program
GPS	Global Positioning System
MC	Mozambique Channel
MRC	Mozambique Ridge Current
NMC	Northern Mozambique Channel
NOAA	National Oceanic and Atmospheric Administration
SEC	Southern Equatorial Current
SMC	Southern Mozambique Channel
SSH	Sea Surface Height
SVPBW	Surface Velocity Program Barometer and Wind
SVPB	Surface Velocity Program Barometer
SVP	Surface Velocity Program
WGS84	World Geodetic System 1984
ADCP	Acoustic Doppler Current Profiler
FLNG	Floating Liquefied Natural Gas
IQR	Interquartile Range

NEMC	Northward East Madagascar Current
Parcels	Probably A Really Computationally Efficient Lagrangian Simulator
Real drifter	Representation of SVP, SVPB and SVPBW real drifter from GDP
SEMC	Southward East Madagascar Current
SLA	Sea Level Anomaly
SST	Sea Surface Temperature
VGD	Virtual Geostrophic Drifter
VGED	Virtual Geostrophic-Ekman Drifter
WIO	Western Indian Ocean
XBT	Expendable Bathythermograph

Chapter 1: INTRODUCTION

Studies from the 1970s to the 1990s utilised various oceanographic techniques. The water structure was analysed using temperature-salinity diagrams to identify water masses and dynamic topography relative to reference levels to track surface circulation patterns (Harris, 1972; Sætre & Da Silva, 1984). Empirical Orthogonal Functions (EOF) analysis of Expendable Bathythermograph (XBT) data collected along shipping routes documented variability in geostrophic transport (Donguy & Meyers, 1995), while SVP drifters and ship drift data were used to observe surface currents and mesoscale features (Gründlingh, 1987; Sætre, 1985). Additionally, infrared satellite imagery was employed to capture large-scale circulation patterns, offering the flow characteristics between the Mozambique and Agulhas Currents (Gründlingh, 1993).

The circulation in the Mozambique Channel (MC) is more complex than a single southward flow, with both the MC and Agulhas current system forming a continuous front (Harris, 1972). Later studies described circulation in the Northern Mozambique Channel (NMC) to be primarily dominated by an anticyclonic pattern (Sætre & Da Silva, 1984) closely linked to the northern monsoon regime (Donguy & Meyers, 1995). In contrast, the Central Mozambique Channel (CMC) was characterised by weak northerly currents that lack directional stability (Sætre, 1985). During three cruises of the *R.V. Meiring Naudé* in the austral summer of 1979-1980, two eddies were identified simultaneously (Gründlingh, 1987). An unexpected advantage occurred when SVP drifters extended the ship's coverage and suggested the presence of the Mozambique Ridge Current (MRC), a westward-flowing current across the NMC curving in an *S* shape over the Mozambique Ridge. Later, it was discovered to be a simultaneous occurrence of a cyclonic and anticyclonic eddy (Gründlingh, 1989), with a continuation of intense Mozambique Current into the Agulhas Current on winter (Gründlingh, 1993).

With short-term data, these studies revealed the complexity of MC's surface circulation influenced by mesoscale eddies, variable currents, and seasonal effects. Utilising SVP drifters, satellite altimetry geostrophic currents and numerical models, post-2000 studies have confirmed previous evidence of large anticyclonic eddies penetrating southwards connected to the variability of the transport by South Equatorial Current (SEC) in the NMC (Backeberg & Reason, 2010; DiMarco et al., 2002; Schouten et al., 2003), influenced by local winds under the influence of the Northern Indian Ocean monsoons (Langa & Calil, 2020). Specifically, in the NMC Rossby waves generate eddies at a rate of seven per year, which slow to five per year as they gain energy moving into the central region and, upon reaching the south, these eddies merge with others from near southern Madagascar, reducing mesoscale activity to four per year before being funnelled into the Agulhas Current (Schouten et al., 2002a, 2002b, 2003; Tew-Kai & Marsac, 2009). Approximately 70% of eddies in the MC are observed to move southwestward into the Agulhas Current system, exhibiting spatial scales

and propagation speeds of roughly 300–350 km and 3–6 km day^{-1}, respectively (Backeberg et al., 2008). Later, with long-term observation was confirmed the channel-sized eddies migrating southward (Harlander et al., 2009), adding the discontinuation of the boundary current in the MC (Swart et al., 2010). Although much later, based on a 25-year simulation of circulation in the Mozambique Channel, supplemented by limited observations from satellite data and current meter moorings, the conclusion was a continuous western boundary current along the Mozambican shelf edge. However, this sporadic event typically lasts only for a short period (Lutjeharms et al., 2012).

It is evident that surface MC circulation is mainly composed of various forces and processes, and the main processes are generally known as geostrophic currents (Hancke et al., 2014), Ekman currents (Ternon et al., 2014b) and Stoke drift relevant to particle dispersion. Those processes tremendously impact larval dispersion, oil spills, and suspended marine debris. Recent studies utilising Surface Velocity Program (SVP) from Global Drifter Program (GDP) have highlighted the contribution of forces on ocean global microplastics accumulation (Onink et al., 2019), described eddies and surface velocities on the MC (Hancke et al., 2014; Ullgren et al., 2016), produced new ocean surface velocity field (a combining geostrophic and Ekman product) (Rio et al., 2014), assessed accuracy and improved Rio et al. (2014) ocean surface velocity product (Hart-Davis et al., 2018; Mulet et al., 2021), and used with lagrangian particle tracking model to highlight the potential usefulness in enhancing search and rescue operations (Hart-Davis & Backeberg, 2021).

Satellite altimeters effectively track eddy movements but must be integrated with high-resolution in-situ observations from surface drifters (Hancke et al., 2014). In the MC, mesoscale features show better alignment with drifter trajectories (Backeberg et al., 2014). When compared to satellite altimetry techniques, the tools used in data collection through surface drifters can provide information with both spatial and temporal resolutions that are considerably more detailed and accurate (Zheng et al., 2015).

This study examined the role of geostrophic-only and combined geostrophic and Ekman currents derived from satellite altimeter observations, wind from numerical models and in-situ observations from SVP drifters in characterising surface current dynamics around Eastern Madagascar Coast (EMC) and MC. Studies have used a Lagrangian particle tracker model known as Parcels (*Probably A Really Computationally Efficient Lagrangian Simulator*) from Lange and van Sebille (2017) to simulate the trajectories of SVP drifters in the Western Indian Ocean (WIO) (Hart-Davis & Backeberg, 2021; Hart-Davis et al., 2018). However, a simple Lagrangian particle tracking model was created from scratch to evaluate the role of the two velocity fields. The examination compared in detailed particle tracking model outputs calculated from the velocity fields with the SVP drifters.

1.1 Research problem

The study of ocean currents from in-situ observations remains reliable. SVP drifters are essential in providing more detailed analysis of complex interactions and validating satellite data at a higher level of detail and accuracy (Zheng et al., 2015).

In the MC, dynamics into surface circulation within the channel was analysed with 60 SVP drifters during the period from 2000 to 2010 (Hancke et al., 2014). One significant finding was that a specific drifter navigated within the frontal zones between eddies without being entrained into the eddies themselves. Another interesting fact was that a specific drifter travelled the length of the MC from North to South in 51 days, while those trapped in eddies took an average of 278 days. Although, 278 days result from an estimated eddy meridional transport of 6 km day^{-1} from Schouten et al. (2003). Notably, drifters moved out of eddies and transitioned between counter-rotating eddies during intense wind events (Hancke et al., 2014). Another study highlighted that satellite altimeter geostrophic currents might be underestimated by as much as 30% in the MC, and ageostrophic components of circulation are significant in the southeastern sector of the Channel near Madagascar (Ternon et al., 2014b). The discrepancies in satellite-derived geostrophic currents are likely due to errors in satellite altimetry measurements near the coast. Similarly, moderate to intense wind events can significantly impact surface currents, diminishing the dominance of geostrophic forces (Ternon et al., 2014b).

The analysis of 22 years of SVP drifters from 1993 to 2015 using Parcels revealed that the combination of geostrophic and Ekman velocity fields underestimated ocean velocity by 27% across the entire Western Indian Ocean (WIO) region, and 35% for MC (Hart-Davis et al., 2018). However, current velocity fields underestimate ocean velocities, necessitating a more thorough examination. This includes a deeper evaluation of the EMC, NMC, CMC, and SMC sub-regions around Madagascar and the Mozambique Channel. Furthermore, an analysis focusing on geostrophic-only and geostrophic+Ekman surface velocity fields is required. To further evaluate in detail, the following questions will be answered:

1. Which velocity field adequately describes the surface circulation around Madagascar and MC?
2. How does the particle tracking model describe the movement of drifters inside a moving eddy in the MC?
3. What factors might surface velocity circulation influence regarding the spread of debris from gas exploration hazards in the NMC?

Accurate ocean current characterisation is vital for search and rescue operations, larval dispersion, oil spills, and suspended marine debris (Hart-Davis & Backeberg, 2021).

1.2 Research objectives

Main objectives

- Evaluate the role of geostrophic and combined geostrophic and Ekman currents in characterising surface circulation around the Madagascar coast and Mozambique Channel.

Specific objectives

- Calculate trajectories of virtual drifters from 2000 to 2019 at SVP drifter's initial position by incorporating Lagrangian parameterisations that tend to follow the virtual velocity fields;
- Describe trajectories and velocities of virtual drifters within moving eddies;
- Determine distances travelled by virtual drifters released inside an area offshore of Cabo Delgado Coast in the NMC.

Chapter 2: LITERATURE REVIEW

2.1 Mozambique Channel Circulation

The Mozambique Channel, between Madagascar and mainland Africa, plays a key commercial route between the Cape of Good Hope and the Northern Indian Ocean (*Figure 2.1*). The flow in the Channel is generally believed to contribute to the strong Agulhas Current further south, though earlier research points to significant interannual variability (DiMarco et al., 2002).

2.1.1 Atmosferic mechanism

The monsoonal wind system affects the northern Mozambique Channel, with wind stress mainly coming from the north to northeast during the austral summer and from the south to southeast during the austral winter (Donguy & Meyers, 1995; Sætre & Da Silva, 1984). The influence of the monsoon winds in the Mozambique Channel diminishes around 20°S. South of this latitude, southeasterly trade winds prevail nearly year-round and are not conducive to Ekman upwelling along the Mozambican coast (Tomczak & Godfrey, 1994). *Figure 2.1* illustrates the monthly mean wind stress (vectors) and wind stress curl (shading) within the Mozambique Channel and around Madagascar for different seasons. January (*Figure 2.1a*) represents typical austral summer conditions aligned with the boreal North East Monsoon (NEM) regime. April (autumn; *Figure 2.1b*) captures the transition from the NEM towards the austral South East Monsoon (SEM), which is depicted in July (austral winter; *Figure 2.1c*). October (*Figure 2.1d*) shows the reversal of the monsoon from the SEM back to the NEM (Vinayachandran et al., 2021).

Wind stress curl can cause Ekman pumping, leading to upwelling (blue areas) and downwelling (red areas) (*Figure 2.1*). The strongest upwelling is predicted around Madagascar, especially in July and October. The upwelling in the southern part of the Mozambique Channel is more variable in location. Hotspot regions include the Sofala Bank, Ponta Zavora, Inhambane, and the Delagoa Bight near Maputo (Roberts et al., 2014). Upwelling in the Mozambique Channel is due to two dynamic forcing mechanisms: local oceanic circulation characteristics and atmospheric wind forcing transferring momentum into the ocean's interior (Malauene et al., 2014).

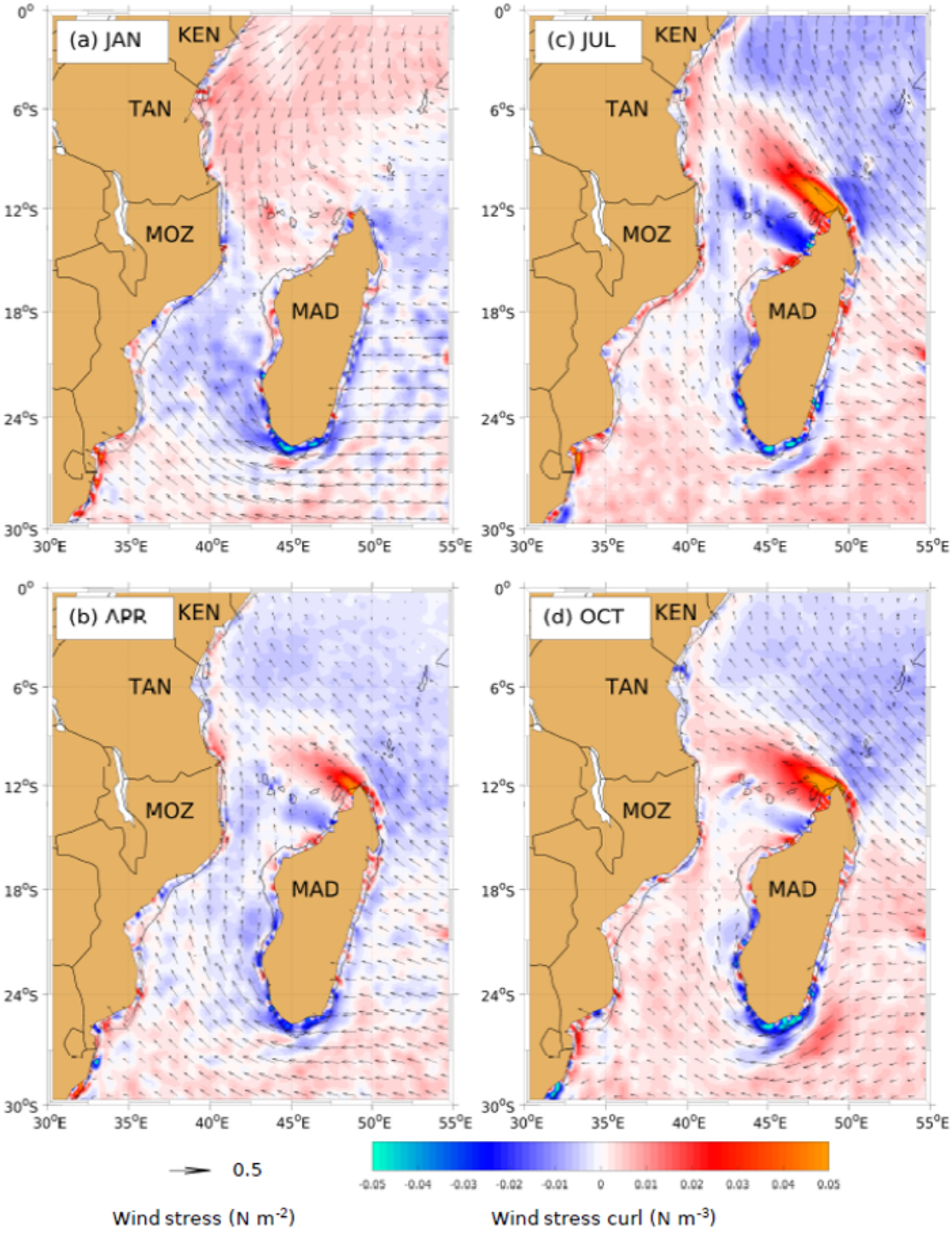

Figure 2.1: *Climatological monthly means of wind stress (vectors) and wind stress curl (shading) are shown for different seasons: austral summer (a, JAN), autumn (b, APR), winter (c, JUL), and spring (d, OCT). Negative (blue) and positive (red) wind stress curls indicate areas favourable for upwelling and downwelling, respectively. The data were sourced from the Scatterometer Climatology of Ocean Winds (SCOW), as described by Risien and Chelton (2008), with a global spatial grid resolution of 1/4° × 1/4°, estimated from 10 years (September 1999 to August 2009) using measurements from QuikSCAT. Figure from Vinayachandran et al. (2021).*

2.1.2 Mesoscale eddies

The SEC, located between 10°S and 20°S, has a total westward transport of approximately 50 Sv (Schouten et al., 2003). At around 17°S, the flow splits into the northward Northeast Madagascar Current (30 Sv) and the southward Southeast Madagascar Current (20 Sv) (*Figure 2.2*). Northwest of Madagascar, the SEC extends to the African coast near 11°S, where it bifurcates into the northward East African Coastal Current (EACC) and a southward flow into the NMC (Backeberg & Reason, 2010).

The MC flow is characterised by southward-moving anticyclonic eddies with spatial scales of around 300–350 km, travelling at speeds of approximately 3–6 km day^{-1} (Backeberg et al., 2008). These eddies interact with the Mozambique Current, creating strong currents and transporting about 15 Sv southward. In April 2000, a southward transport of around 30 Sv was recorded at 12°S near the African coast, consisting of water similar to that found in the EACC (De Ruijter et al., 2002).

The eddies in the CMC have greater kinetic energy due to larger diameters, averaging 300 km compared to 100 km in the northern region (Backeberg et al., 2008). Further south, eddies within the Channel merge with those formed south of Madagascar near 28°S, contributing with energy, momentum, and possibly water masses to the Agulhas Current. The South East Madagascar Current (SEMC) retroflects southwest of Madagascar, generating cyclonic and anticyclonic eddies with diameters up to 250 km, which propagate southwestwards towards the Agulhas Current (Halo et al., 2014). Although the MC eddies and the EMC do not form a direct continuum with the Agulhas Current, they significantly influence its dynamics and contribute to the fluxes of volume, heat, and salt (Backeberg et al., 2008).

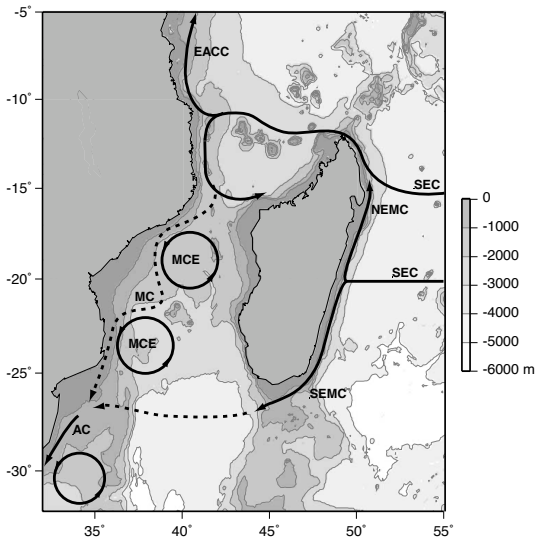

Figure 2.2: *Bathymetry around Madagascar and the Mozambique Channel, along with the main currents and flow features. Figure from Schouten et al. (2003).*

2.2 Geostrophic and Ekman flow

2.2.1 Geostrophic currents

Measuring ocean currents accurately is complex and expensive. In shallow and deep waters, a current meter could be anchored with a weight at the bottom and a buoy at the surface in order to measure currents at specific depths. However, this method only provides information about the currents at the specific point where the meter was anchored. Although, nowadays, Acoustic Doppler Current Profilers (ADCPs) are commonly deployed on moving boats to measure velocity distributions and discharge in oceans, estuaries, rivers, and streams. This method is still expensive, especially when anchoring in the deep ocean, which is more challenging.

As discussed by Talley et al. (2011), the pressure gradient force points from high to low pressure. In a non-rotating flow, water moves from high to low pressure. With rotation, the Coriolis force opposes the pressure gradient force, resulting in zero net force. The water parcel moves perpendicular to both forces. In geostrophic flow, the pressure gradient force pushes the water parcel from high to low pressure, while the Coriolis force moves the parcel to the right in the Northern Hemisphere or the left in the Southern Hemisphere. In a "word" equation, geostrophic balance is *horizontal Coriolis acceleration = horizontal pressure gradient force*.

In the ocean's interior, away from the top and bottom Ekman layers, horizontal pressure gradients balance the Coriolis force resulting from horizontal currents over large horizontal distances and time periods, a state known as geostrophic balance (Stewart, 2008). The geostrophic balance is a result of equations of motion without friction. It is assumed that the flow has no acceleration $\frac{du}{dt} = \frac{dv}{dt} = \frac{dw}{dt} = 0$ and that horizontal velocities are much larger than vertical, which may be neglected (Pond & Pickard, 1983). Also, the friction terms are neglected $F_x = F_y = F_z = 0$. The mathematical expression of equations of motions in the cartesian coordinate system are:

$$\begin{cases} \text{X:} & \dfrac{\partial u}{\partial t} + u\dfrac{\partial u}{\partial x} + v\dfrac{\partial u}{\partial y} + w\dfrac{\partial u}{\partial z} = -\dfrac{1}{\rho}\dfrac{\partial p}{\partial x} + 2\Omega v \sin\phi + F_x \\ \text{Y:} & \dfrac{\partial v}{\partial t} + u\dfrac{\partial v}{\partial x} + v\dfrac{\partial v}{\partial y} + w\dfrac{\partial v}{\partial z} = -\dfrac{1}{\rho}\dfrac{\partial p}{\partial y} - 2\Omega u \sin\phi + F_y \\ \text{Z:} & \dfrac{\partial w}{\partial t} + u\dfrac{\partial w}{\partial x} + v\dfrac{\partial w}{\partial y} + w\dfrac{\partial w}{\partial z} = -\dfrac{1}{\rho}\dfrac{\partial p}{\partial z} - g + F_z \end{cases} \tag{2.1}$$

Where F_i are the components of any frictional force per unit mass, ϕ is latitude, and Coriolis parameter $f = 2\Omega \sin\phi$ does not act in the vertical direction (Z component). Applying the assumptions of geostrophic

balance, the result becomes:

$$\begin{cases} \text{(a)} & \dfrac{\partial p}{\partial x} = \rho f v \\ \text{(b)} & \dfrac{\partial p}{\partial y} = -\rho f u \\ \text{(c)} & \dfrac{\partial p}{\partial z} = -\rho g \end{cases} \tag{2.2}$$

Ocean pressure increases with greater water mass above, while sea surface pressure differences are due to water bulging in relation to the geoid (Talley et al., 2011). The geostrophic velocities at the sea surface could be calculated if the appropriately time-averaged sea surface height is known, and satellite altimetry can provide this information. The geostrophic velocity at the sea surface in terms of sea surface height η above a level surface is derived from *Equation 2.2* and has the form:

$$\begin{cases} \text{(a)} & u^0_{\text{geo}} = -\dfrac{g}{f}\dfrac{\partial \eta}{\partial y} \\ \text{(b)} & v^0_{\text{geo}} = \dfrac{g}{f}\dfrac{\partial \eta}{\partial x} \end{cases} \tag{2.3}$$

2.2.2 Ekman transport

In the open ocean, the second major contribution to the ocean surface currents after geostrophic is the Ekman response of the ocean to wind stress (Rio et al., 2014). The theoretical foundations for Ekman's transport are well known and come from a concept that steady winds blowing on the sea surface produce a thin, horizontal boundary layer called the *Ekman layer* (Stewart, 2008).

Wind stress is transmitted to the ocean's surface layer through frictional processes that extend several tens of metres into the ocean (Talley et al., 2011). On timescales longer than a day, the response of this layer is strongly influenced by the Coriolis acceleration. This wind-driven frictional region is known as the Ekman layer, where the primary physical processes are friction (eddy viscosity) and Coriolis acceleration (Stewart, 2008). The velocity within the Ekman layer is strongest at the sea surface and decays exponentially with depth, becoming negligible at approximately 50 m (Talley et al., 2011). Ekman currents are the ocean's response to surface wind stress in a rotating frame with increasing depth (Ekman, 1905). The net transport integrated through the Ekman layer is precisely to the right of the wind direction in the Northern Hemisphere and to

the left in the Southern Hemisphere. Due to the acceleration of the Coriolis force, the surface water in an Ekman layer moves at an angle to the wind. However, in the Ekman depth, the water velocity is 4% and moves opposite to the one on the surface. Although the Ekman layer coexists with the mixed layer depth and the euphotic zone depth, it is distinct from them (Talley et al., 2011).

From the equations of motion (*Equation 2.1*) omitting geostrophic balance and keeping friction terms, the horizontal part becomes the Ekman equations, where there is a balance between Coriolis and friction terms:

$$\begin{cases} \text{(a)} \quad 0 = f v_E + \dfrac{1}{\rho}\dfrac{\partial \tau_x}{\partial z} \\ \\ \text{(b)} \quad 0 = -f u_E + \dfrac{1}{\rho}\dfrac{\partial \tau_y}{\partial z} \end{cases} \tag{2.4}$$

Where v_E and u_E are the meridional and zonal components of the Ekman transport. f is Coriolis parameter. τ_x and τ_y are the zonal and meridional components of the wind stress, which as the form $\rho_a C_D \left(u^2 + v^2\right)^{\frac{1}{2}} u$ and $\rho_a C_D \left(u^2 + v^2\right)^{\frac{1}{2}} v$ respectively. ρ_a is the air density, u and v are the zonal e meridional components of wind velocity estimated 10 m above sea level.

The variability of the wind blowing across the sea surface causes variability in the Ekman transports. Due to the conservation of mass, this spatial variability in transports leads to vertical velocities at the bottom of the Ekman layer (Stewart, 2008). Integrating the continuity equation $\left(\frac{\partial u}{\partial x} + \frac{\partial v}{\partial y} + \frac{\partial w}{\partial z} = 0\right)$ with respect to vertical from surface until the Ekman depth, the Ekman pumping gains form:

$$w_E = \frac{1}{\rho f}\left[\frac{\partial}{\partial x}(\tau_y) - \frac{\partial}{\partial y}(\tau_x)\right] \tag{2.5}$$

The terms inside square brackets (*Equation 2.5*) are the wind stress curl, where positive values are upwelling, and negative values are downwelling.

2.3 Global Drifter Programme

A drifting object with a surface float measures velocities affected by surface drift, Stokes drift, and direct wind force. Because of the strong vertical shears near the surface caused by wind and waves, different designs of surface floats can exhibit significant variations in their ability to follow water movements. To minimise motion caused by surface-wave-driven Stokes layer and to avoid the effects of wind, drifters are typically equipped with a sea anchor, or drogue, placed at a specific depth below the surface (Lumpkin et al., 2017).

In 1982, the World Climate Research Program recognised the need for a global network of drifters to enhance oceanographic and climate research (Lumpkin & Pazos, 2007). Challenges included uncertainties, significant variations in drifter designs, and high costs and excessive weight of some types. To address this, the program called for a standardised, low-cost, lightweight, and easily deployable surface drifter with a semi-rigid drogue capable of maintaining its shape in high-shear flows.

By 1993, a definitive SVP drifter design was established by combining the holey-sock drogue from Atlantic Oceanographic and Meteorological Laboratory (AOML) drifters with reinforced tether ends and surface float designs from Scripps Institution of Oceanography (SIO), becoming the cornerstone for all subsequent SVP drifter development (Lumpkin & Pazos, 2007).

Today, the array of SVP drifters is collectively known as the Global Drifter Program (GDP), a component of NOAA's Global Ocean Observing System (GOOS) and Global Climate Observing System (GCOS), as well as a scientific project of the Data Buoy Cooperation Panel (DBCP) under the World Meteorological Organization and the International Oceanographic Commission (IOC) (Lumpkin & Pazos, 2007). The GDP's scientific objectives are to provide operational, near-real-time observations of surface velocity, Sea Surface Temperature (SST), and sea level pressure for numerical weather forecasting, research, and in-situ calibration/verification of satellite observations (Lumpkin & Pazos, 2007).

There are two main sizes of SVP drifters (*Figure 2.3*): the original, larger model and a newer, more streamlined "mini" version. Several manufacturers produce the mini drifter alongside the original-sized SVP drifters (Lumpkin & Pazos, 2007). The surface float of an SVP drifter can vary in diameter from 30.5 cm for the smallest mini to 40 cm. Initially, the surface float hull was constructed using fibreglass 0.3–0.4 cm thick. The SVP drifter's surface float contains battery packs, a satellite transmitter, a thermistor, and instruments to measure barometric pressure, wind speed, direction, salinity, and ocean colour (Lumpkin & Pazos, 2007). It also has a submergence sensor to detect if the drogue has been lost.

2.3.1 Drifters dataset

Historical observations, dating back to 1979, have been processed step by step to create a 6-hour joint dataset of drifter positions, velocities, and SST estimates, including uncertainty measures (Elipot et al., 2016). As the

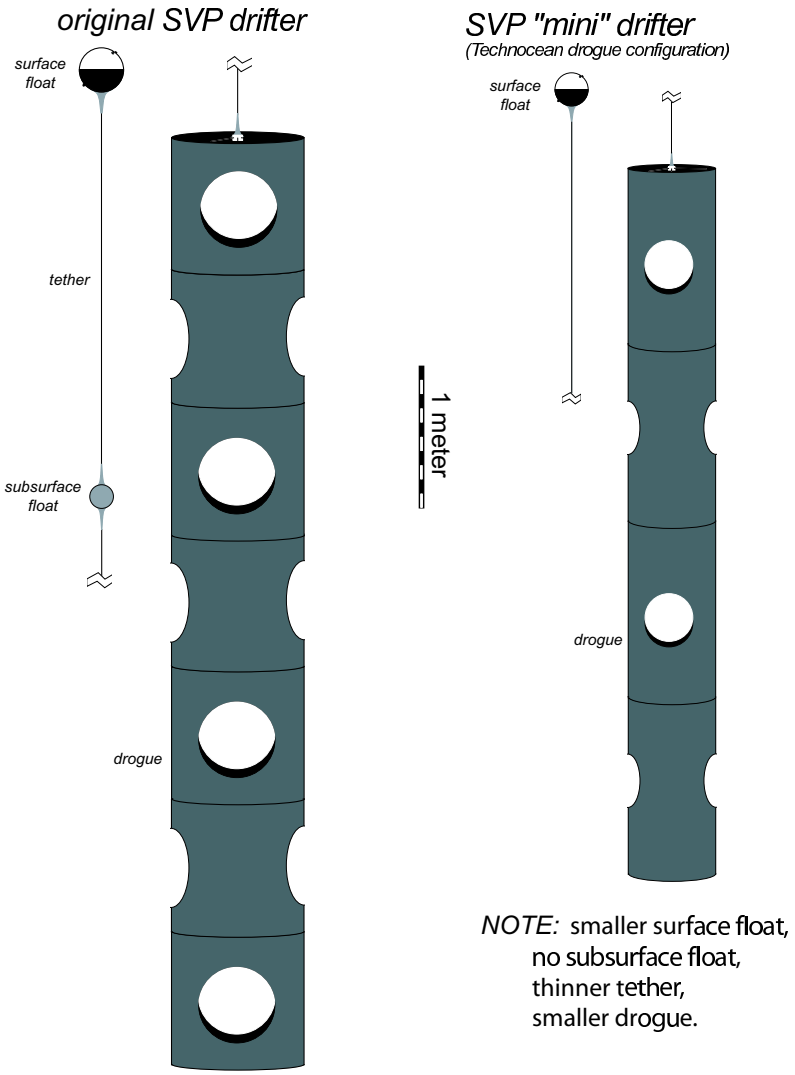

Figure 2.3: *Schematic view of two SVP drifter types shown to scale; most of the tether length has been excluded. The drogues are centred at a depth of 15 m. Figure from Lumpkin and Pazos (2007).*

frequency of drifter observations has increased since the array's implementation, a new methodology was introduced in 2016 to generate an hourly product of drifter velocity estimates with uncertainties (Elipot et al., 2022b).

To identify the most suitable interpolation method for the global dataset position, and velocities, Elipot et al. (2016) tested four different techniques using the Salinity Processes in the Upper Ocean Regional Study (SPURS) dataset. The Data Assembly Center (DAC) currently employs the first method, Kriging, to produce the 6-hourly GDP product. They adapted this method for hourly time steps to serve as a benchmark for comparing other methods. The second method is an enhanced version of simple linear interpolation that accounts for the Earth's curvature, referred to as "spherical linear interpolation". The linear interpolation in

the analysis was included because it is simple and widely utilized, providing a baseline expectation that more advanced methods should outperform it. The third and fourth methods are "weighted maximum likelihood estimates" which involve locally modelling drifter coordinates as linear functions of time—representing a conceptual advancement over basic linear interpolation.

The method for SST defines four levels of data, labelled Level-0, 1, 2, and 3, as follows (Elipot et al., 2022b):

- Level-0 represents the original, unevenly distributed data as recorded by the SST sensor and transmitted to the GDP via the Service Argos system or the Lagrangian Drifter Laboratory at Scripps Institution of Oceanography.
- Level-1 results from initial processing and quality control applied to the Level-0 data.
- Level-2 corresponds to SST estimates at the exact unevenly distributed times as the Level-1 data.
- Level-3 consists of SST estimates at regular hourly intervals, aligned with the position and velocity estimates for drifters in the GDP hourly dataset.

Preliminary analysis of the drifter velocity variance indicates that this new dataset offers potential as a valuable tool for studying small-scale, high-frequency oceanic processes (Elipot et al., 2016). In particular, velocity rotary spectra suggest that high-frequency tidal and internal wave motions can be detected on a global scale.

Table 2.1: *Table of location, velocity, and temperature data products and availability from the GDP which defines three levels of data processing. Variables without asterisks are observations, while variables with asterisks are estimates. Only Level-3 data products are readily available from the GDP. Adapted from Elipot et al. (2022b).*

	Argos drifters		**Iridium drifters**	
	Location (X, Y) & velocity (U, V)	**Temperature (T)**	**Location (X, Y) & velocity (U, V)**	**Temperature (T)**
Level-1	X, Y	T	X, Y	T
Level-2	—	T* Elipot et al. (2022b)	X*, Y*, U*, V* Elipot et al. (2016)	T* Elipot et al. (2022b)
6-hourly Level-3	X*, Y*, U*, V*	T*	X*, Y*, U*, V*	T*
Hourly Level-3	X*, Y*, U*, V* Elipot et al. (2016)	T* Elipot et al. (2022b)	X*, Y*, U*, V* Elipot et al. (2016)	T* Elipot et al. (2022b)

Chapter 3: DATA AND METHODOLOGY

This chapter is organised into four sections as follows:

1. Area of study (section 3.1): provides a brief introduction to the WIO region and specific MC and EMC area of study.

2. Surface drifter observations (section 3.2): details the GDP SVP drifter data used in the study.

3. Velocity fields from from satellite altimeter observations, wind from numerical models and in-situ observations from SVP drifters (section 3.3): presents and describes the velocity fields dataset from the Copernicus Marine Environment Monitoring Service (CMEMS).

4. Particle tracking model (section 3.4): covers the velocity field conversion and describes the model.

3.1 Area of study

The study area depicted in *Figure 3.1* focuses on the WIO region, specifically the MC. The area of interest is outlined in black sub-region boxes, encompassing key countries within this zone, including Mozambique, Tanzania, Madagascar and South Africa. This figure was divided into four main sub-regions for detailed analysis. Eastern Madagascar Coast (EMC), Northen Mozambique Channel (NMC), Central Mozambique Channe (CMC) and Southern Mozambique Channel (SMC). The concept of dividing the area of interest into four sub-regions was to highlight the dynamics of each region.

Several major ocean currents heavily influence the Western Indian Ocean region. One of the significant currents is the SEC, which flows westward and splits near the EMC. A part of it turns south, creating the Southeast Madagascar Current, while the remainder contributes to the formation of the Mozambique Eddies. These eddies are a series of cyclonic and anti-cyclonic patterns within the Mozambique Channel.

Further south, the Agulhas Current, flowing along the southeast coast of Africa, continues towards the Southeast Atlantic Ocean. The retroflection of this current near the southern tip of the African continent leads to the formation of the Agulhas Return Currents, a significant feature in the Southern Hemisphere's ocean circulation.

The MC transports warm tropical waters southward and creates a dynamic environment with variations in sea surface height, temperature, and salinity (Vinayachandran et al., 2021). The Channel's features influence local and regional oceanographic processes, making it a hotspot for marine biodiversity and a key area for studying ocean-atmosphere interactions in the Western Indian Ocean (Ternon et al., 2014a).

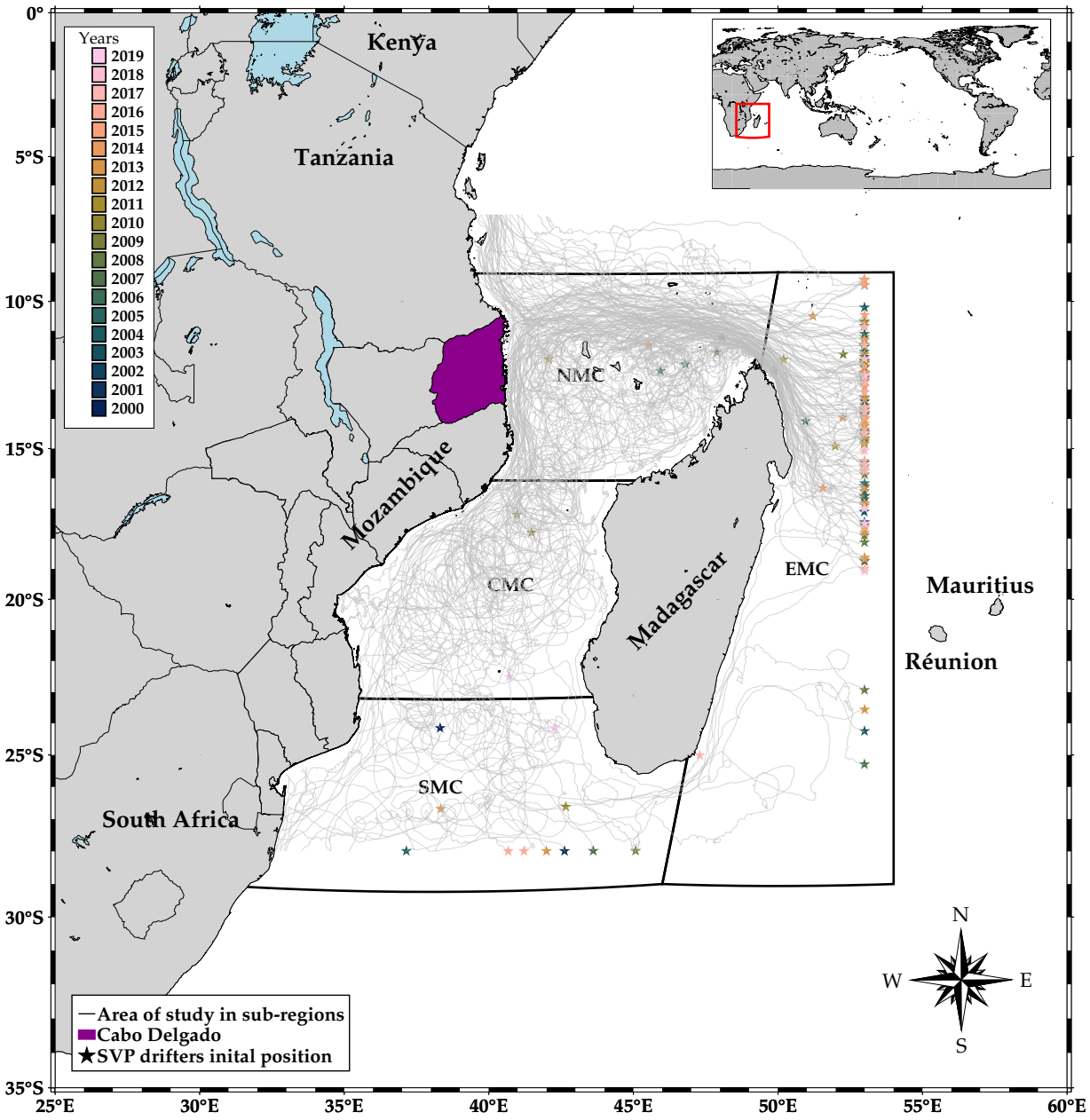

Figure 3.1: *West Indian Ocean, where black box represents the area of study in sub-regions Eastern Madagascar Coast (EMC), Northern Mozambique Channel (NMC), Central Mozambique Channel (CMC) and Southern Mozambique Channel (SMC). The stars represent SVP drifter initial position. The grey transparent lines are SVP drifter tracks. Cabo Delgado is represented for the purpose of demonstrating the province where natural gas is explored offshore. Created with PyGMT (Tian et al., 2024). Adapted from Hart-Davis et al. (2018).*

3.2 Surface drifter observations

A global surface drifter dataset was used as a real drifter at hourly resolution. The dataset is from GDP, which is part of NOAA's Global Ocean Observing System (Elipot et al., 2016). The GDP plays a crucial role in gathering on-site data about ocean surface temperatures and currents (Elipot et al., 2022b). This information, along with the positions of drifters, is then transmitted using the Argos satellite system (Hart-Davis et al., 2018). The Global Positioning System (GPS) is increasingly utilised to track drifters. This modern system offers exact drifter locations at meter-scale accuracy and provides data on an hourly basis or even shorter intervals (Elipot et al., 2022b).

The main instrument is an SVP drifter that features a hull centred at 15 m depth to measure mixed layer currents, made of acrylonitrile butadiene styrene (ABS) and employs a rip-stop fabric nylon drogue tethered with a steel wire-rope (Lumpkin & Pazos, 2007; Niiler, 2001). It integrates a thermistor in a thermally insulated stainless-steel enclosure for accurate sea surface temperature readings corrected for thermal biases (Said et al., 2013). Additionally, variants like the SVPB and SVPBW drifters include atmospheric pressure sensors and wind speed measuring capabilities.

The selection of drifters was observed during the 20-year analysis period. A total of 635 drifters passed through MC, specifically the area of interest (*Figure 3.1*), between 2000 and 2019. Most drifters had inconsistent time intervals, gaps in some parameters, sensor faults, and lost drogues. These issues led to the selection of only 151 drifters passing through the area of interest during the period. Trajectories of drifters that retained their drogues were selected to ensure high data quality. Despite this selection, the analysis also included most drifters with lost drogues. For specific details about these drifters, please refer to *Table 3.1*. Although drifters that retained their drogues are considered reliable representations of ocean currents, using drifters with lost drogues is necessary to assess instantaneous ageostrophic components. The absence of the drogue could lead to wind slippage, which alters the drifter's trajectory and introduces biases in velocity estimations (Said et al., 2013).

The annual distribution is described in *Figure 3.2*. In 2014, a maximum of 21 drifters passed through the area of interest, followed by 17 in 2015 and fewer than 12 in the remaining years. This figure highlights that most drifters were released in the Eastern Indian Ocean, and only 19 out of 151 were released inside MC.

Table 3.1: *Details SVP drifter passed through MC during 2000 to 2019 period.*

Drifter type	Dataset	Total number of drifters	Number of drifters with drogue lost			Source
			Before domain	Inside domain	After domain	
SVP	Elipot et al. (2022a)	47	28	10	9	Elipot et al. (2016, 2022b)
SVPB	Elipot et al. (2022a)	103	60	29	14	Elipot et al. (2016, 2022b)
SVPBW	Elipot et al. (2022a)	1	0	0	1	Elipot et al. (2016, 2022b)
Total		**151**	**88**	**39**	**24**	

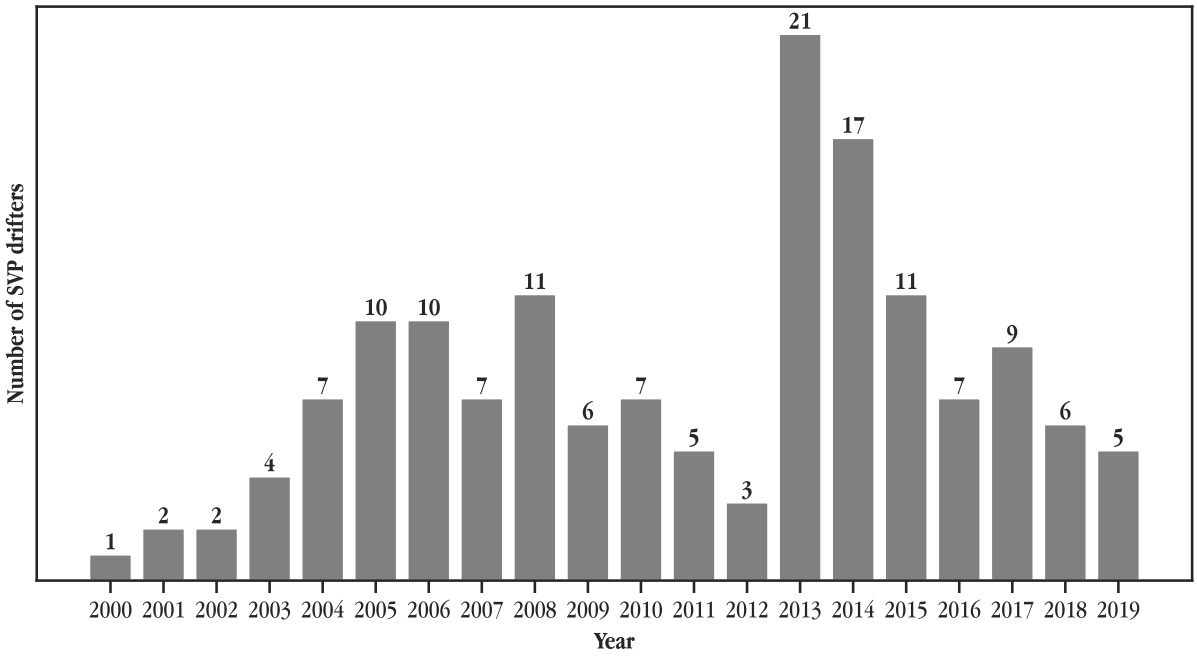

Figure 3.2: *Annual distribution of SVP drifters between 2000 and 2019. The number of drifters each year is shown above the bars.*

3.3 Velocity fields

Accurate satellite altimeter systems are essential for measuring surface oceanic topography. Early missions aboard Seasat, Geosat, ERS-1, and ERS-2 were designed to monitor the week-to-week variability of ocean currents (Stewart, 2008). The launch of the TOPEX/Poseidon in 1992, followed by Jason-1 in 2001 and Jason-2 in 2008, enabled more precise measurements to observe permanent surface circulation, tides, and the variability of gyre-scale currents. Before approximately 2004, limited local knowledge of the geoid meant altimeters were typically flown in orbits with exactly repeating ground tracks; thus, TOPEX/Poseidon and Jason satellites retrace the same ground track every 9.9156 days. By subtracting sea-surface height measurements from consecutive passes along the same track, changes in ocean topography can be observed without precise knowledge of the geoid (Stewart, 2008). Since the geoid remains constant over time, this method reveals variations caused by changing currents, such as mesoscale eddies ranging from roughly 20 to 500 kilometres in diameter, assuming tidal effects have been removed from the data (Stewart, 2008).

The geostrophic current velocity field is based on reprocessed products from Mulet et al. (2021) and Pujol et al. (2016). This product includes sea level anomaly (SLA) products derived from satellite altimetry over 20 years. Key improvements in the "Delayed-Time" DT2014 version of the Data Unification and Altimeter Combination System (DUACS) include a more extended reference period, updated altimeter standards, improved data processing techniques, and enhanced mesoscale signal representation. The data produced are generated by the processing system, including data from all altimeter Copernicus missions (Sentinel-6A, Sentinel-3A) and other collaborative or opportunity missions (e.g. Jason-3, Saral/AltiKa, Cryosat-2, OSTM/Jason-2, Jason-1, Topex/Poseidon, Envisat, ERS-1/2).

Table 3.2: *Overview of the CMEMS datasets used for particle tracking.*

Velocity field	Dataset	Spatial resolution	Temporal resolution	Source
Geostrophic[1]	European Union-Copernicus Marine Service (2023)	$0.25° \times 0.25°$	Daily	Mulet et al. (2021)
Geostrophic + Ekman[2]	European Union-Copernicus Marine Service (2023)	$0.25° \times 0.25°$	Daily	Mulet et al. (2021)

Notes:
[1] Satellite observations.
[2] Numerical models, In-situ observations, Satellite observations.

The combined geostrophic and Ekman velocity field derived from CNES-CLS18 Mean Dynamic Topography (MDT) combines satellite altimeter, gravity, and in-situ observations to refine the estimation of ocean surface

currents (Mulet et al., 2021). This product utilises advanced datasets, including updated drifter velocities (SVP and Argo floats) and wind data to improve the representation of wind-driven currents. The model incorporates corrections for wind slippage and utilises 3-hourly wind stress data from ERA-Interim at an 80 km resolution. The resulting dataset represents a combined geostrophic current and wind-induced Ekman drift by removing ageostrophic components, including tidal and inertial velocities.

The velocity fields stored at CMEMS (details in *Table 3.2*) were acquired to force the movement of surface virtual drifters. Only surface was used since surface and 15m depth horizontal velocity are available for the combined geostrophic and Ekman currents. The spatial resolution of both datasets is $\frac{1}{4}^{\circ}$, and temporal resolution is daily; to fill the gaps of geographical grid points and timesteps, the linear interpolation equation $f(x) = f(x_0) + \frac{f(x_1)-f(x_0)}{x_1-x_0}(x-x_0)$ described by Noor et al. (2014) was used. Where x is the independent variable, x_1 and x_0 are known values of the independent variable, and $f(x)$ is the value of the dependent variable for a value x of the independent variable.

3.4 Particle tracking model

3.4.1 Particle tracking

Lagrangian trajectories of $U_p = U$ particles within a fluid are accurately described by the *Equation 3.1*. Assuming that the particle velocity U_p is equal to the velocity field U, the equations calculate the updated positions in longitude x and latitude y at discrete time intervals. Specifically, the positional updates are derived by applying the velocities u and v over a time increment Δt, illustrating the continuous movement of particles within the surface two-dimensional velocity field.

$$\begin{cases} X(t+\Delta t) = X(t) + \displaystyle\int_t^{t+\Delta t} u(x,t)\,dt \\ \\ Y(t+\Delta t) = Y(t) + \displaystyle\int_t^{t+\Delta t} v(y,t)\,dt \end{cases} \tag{3.1}$$

The velocity components u and v referred to in equation *Equation 3.1* are sourced from CMEMS. The velocities are expressed in $m \cdot s^{-1}$ (meters per second). The necessary conversion to $deg \cdot s^{-1}$ (degree per second) was made using the expressions from subsection 3.4.2. This conversion is crucial for standardising units in *Equation 3.1* due to the representation of drifter positions from GDP in geographic coordinates deg (degrees), which served as the initial position for the calculation (*Figure 3.1*).

The calculation used two velocity field datasets: geostrophic and combined geostrophic and Ekman (*Table 3.2*). The resulting drifter trajectories are referred to as *virtual drifter*. Specifically, from each dataset, this thesis will refer them as Virtual Geostrophic Drifter (VGD) and Virtual Geostrophic-Ekman Drifter (VGED), respectively. The observed SVP drifter is referred to as the real drifter.

Some applications reintroduce virtual particles in the model domain when they come ashore. This requires implementing a boundary condition. Due to relatively low resolution CMEMS velocity fields, virtual particles often hit the land when they travel close to the shore. This thesis adopts the approach of recording every virtual particle trajectory when it comes ashore. This method enables a detailed examination of the CMEMS velocity fields, facilitating a more precise understanding of its role in characterising the MC circulation.

While alternative particle tracking models, such as that presented by Lange and van Sebille (2017), employ a fourth-order Runge-Kutta discretisation of *Equation 3.1*, this thesis adopts the more straightforward Euler stepping method. The Euler method is computationally efficient and straightforward to implement, which allows for a precise evaluation of the velocity fields. However, it is recognised that Euler stepping, being a first-order method, may introduce more significant numerical errors over time than higher-order methods

like Runge-Kutta.

3.4.2 Velocity conversion

To facilitate coherent and consistent calculations in subsection 3.4.1, conversion of the velocity field was obtained by interpreting *Figure 3.3*. The figure represents a three-dimensional spherical coordinate system, a method for defining the position of a point in three-dimensional space using three coordinates: radial distance r, latitude angle ϕ, and longitude angle λ.

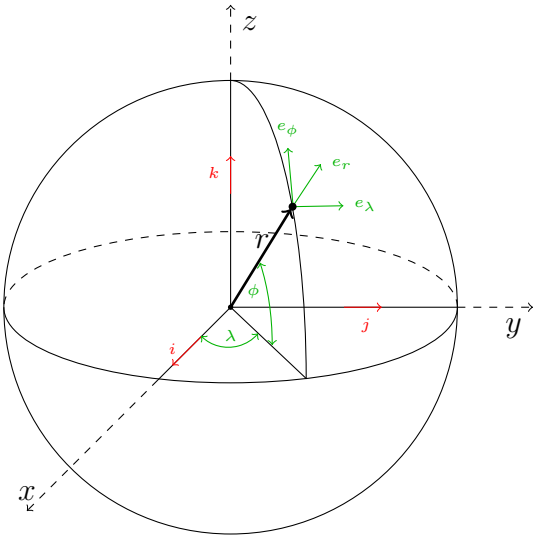

Figure 3.3: *Spherical and cartesian coordinate system, where ϕ is the latitude angle, λ is the azimuthal angle or longitude, and r is the distance from the origin at the centre of the Earth. Adapted from (Constantin & Johnson, 2018).*

The transformation from spherical to cartesian coordinates is fundamental for assimilating terrestrial observations into three-dimensional geospatial models and interoperability with satellite navigation systems (Gerdan & Deakin, 1999). These cartesian coordinates in *Equation 3.2*, x, y, and z, are computed from the geodetic latitude ϕ, longitude λ, and altitude ***alt*** relative to the Earth's reference ellipsoid, which is defined by its eccentricity e. Constants values ν, alt and e are defined by Gerdan and Deakin (1999) and in *Equation 3.2* they represent radial distance r from *Figure 3.3*. The calculation incorporates the prime vertical radius of curvature ν, which is a function of latitude and reflects the non-spherical shape of the Earth (see appendix subsection A.1). This transformation is essential for accurately representing point locations from the ellipsoidal Earth to a Cartesian coordinate plane.

$$\begin{cases} x = (\nu + \text{alt}) \cdot \cos(\phi) \cdot \cos(\lambda) \\ y = (\nu + \text{alt}) \cdot \cos(\phi) \cdot \sin(\lambda) \\ z = [(1 - e^2) \cdot \nu + \text{alt}] \cdot \sin(\phi) \end{cases} \tag{3.2}$$

The primary goal is to determine the relationship for converting a cartesian velocity value from meters per second ($m \cdot s^{-1}$) to degrees per second ($deg \cdot s^{-1}$). The velocity components of a moving particle are found by calculating the total derivatives of the Cartesian coordinates with respect to time, as indicated in equation *Equation 3.3*.

When considering motion in the ϕ-direction, the arc length ds of a small circle segment subtended by a small angle $d\phi$ is given by the equation $ds = r \cdot d\phi$. The linear velocity in the direction of ϕ, denoted as v_ϕ, represents the rate at which the particle moves along this circular path. By definition, velocity is the time derivative of the position (or arc length in this case), therefore $v_\phi = \frac{ds}{dt} = \frac{d}{dt}(r \cdot \phi) = r \cdot \frac{d\phi}{dt}$. At this stage, v_ϕ can be regarded as the velocity component v and substituted into the *Equation 3.3*.

In order to determine the relationship between the linear velocity in the longitude direction λ and its angular rate of change $\frac{d\lambda}{dt}$, a geometric approach similar to what was used for the polar angle ϕ can be employed. However, in this case, consideration needs to be given to the fact that the path travelled in the λ-direction is on a circle at a latitude ϕ. In spherical coordinates, the longitude angle λ measures the position around the axis running through the poles. If a point moves along the surface of a sphere at a constant latitude ϕ, the motion follows a circle parallel to the equator, often referred to as a small circle, with a radius given by $r_\lambda = r \cdot \cos(\phi)$. The arc length ds for a small displacement $d\lambda$ along this small circle is given by the equation $ds = r_\lambda \cdot d\lambda = r \cdot \cos(\phi) \cdot d\lambda$. The linear velocity in the longitude direction v_λ represents the rate at which the point moves along this arc, and can be found as the derivative of the arc length with respect to time: $v_\lambda = \frac{ds}{dt} = \frac{d}{dt}(r \cdot \cos(\phi) \cdot \lambda) = r \cdot \cos(\phi) \cdot \frac{d\lambda}{dt}$. Assuming v_λ is the u velocity component, it is then substituted in the *Equation 3.3*.

$$\begin{cases} \dfrac{dx}{dt} = -u \cdot \sin(\lambda) - v \cdot \cos(\lambda) \cdot \sin(\phi) \\ \dfrac{dy}{dt} = u \cdot \cos(\lambda) - v \cdot \sin(\phi) \cdot \sin(\lambda) \\ \dfrac{dz}{dt} = v \cdot \cos(\phi) \end{cases} \tag{3.3}$$

The Cartesian coordinates in equations *Equation 3.4* are modified to include the velocity components, reflecting movement over one second. This involves updating the x, y, and z coordinates to account for dynamic changes in the system by factoring in the velocity of each component over a one-second interval.

$$\begin{cases} x = 1\mathbf{s} \cdot \dfrac{dx}{dt} + (\nu + \text{alt}) \cdot \cos(\phi) \cdot \cos(\lambda) \\ y = 1\mathbf{s} \cdot \dfrac{dy}{dt} + (\nu + \text{alt}) \cdot \cos(\phi) \cdot \sin(\lambda) \\ z = 1\mathbf{s} \cdot \dfrac{dz}{dt} + [(1 - e^2)\nu + \text{alt}] \cdot \sin(\phi) \end{cases} \tag{3.4}$$

The cartesian coordinates described in *Equation 3.4* are converted into spherical coordinates using the relationships defined in appendix A.2. This conversion requires calculating the differences between the updated values (ϕ_1 and λ_1), which represent the positions after a one-second interval and the initial latitude (ϕ) and longitude (λ) from *Equation 3.2*. The resulting variances are represented in *Equation 3.5*, providing the velocity in degrees per second.

$$\begin{cases} u = \lambda_1 - \lambda \\ v = \phi_1 - \phi \end{cases} \tag{3.5}$$

The two-dimensional velocity field is expressed in degrees per second and can be utilised in *Equation 3.1*.

Chapter 4: RESULTS

Figure 4.1 shows the trajectories of a real and virtual drifters 40551 (VGD and VGED). The real drifter followed a trajectory for 77 days, with a drogue detached before the initial position. This indicates that the surface-following mechanism was lost, which ensures remaining in the water column. Thus, the phenomenon may have been influenced more by wind and waves than by subsurface currents. Consequently, the initial position of real drifter lined up around 53° E (*Figure 3.1*) arises from these tracks being a subset of much larger tracks and primarily deployed in the Eastern Indian Ocean.

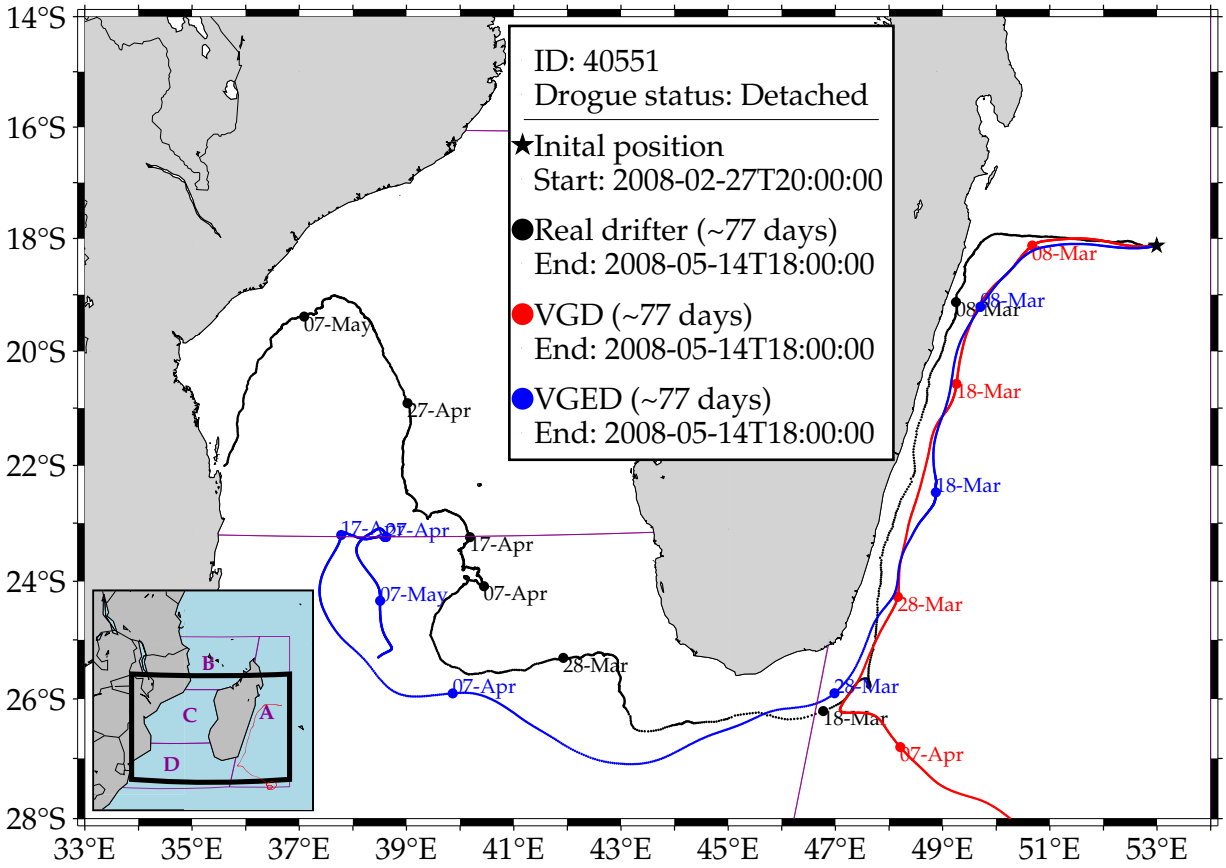

Figure 4.1: *Trajectories of real drifter 40551 and two virtual drifters forced by geostrophic-only and geostrophic + Ekman currents. The real drifter (black) travelled for 77 days with a detached drogue, starting on 27 February 2008 and ending on 14 May 2008. The virtual drifters (VGD - red and VGED - blue) started from the same initial position, following a path for 77 days. The detachment of the drogue occurred prior to entering the domain.*

The virtual drifters started from the same initial position as the real drifter but deviated from the real drifter's trajectories. The VGD follows a course more directly south compared to the real drifter. The VGED trajectory

was nearly similar to that of the real drifter, although complete variability was lacking. The virtual drifter deviated and entered the SMC, while the real drifter went even further. Overall, the real drifter covers a greater distance, meandering westward, even though starting in EMC and eventually entering the CMC through south Madagascar, while the VGED lacks in the distance covered and VGD shows more constrained movement, and a deviation to the southeast. The position of the virtual drifters, compared with the real drifter, shows that in the first 20 days, VGD was much slower than the real drifter, whereas on March 18, the real drifter reached the southern tip of Madagascar while the virtual counterparts were far behind.

Figure 4.2 illustrate the trajectories of real and virtual drifters (VGD and VGED) 46070, with all of them following a 35 days trajectory. Although this drifter had an initial position in EMC, the assumption was made that the drifter was on NMC since the track was mainly in this region. Moreover, the real drifter's drogue was detached before entering the domain, indicating that the device may have been more affected by surface wind and wave action than by subsurface currents. Although the track of the real drifter covers a significant area, a deviation pattern emerges with movement primarily westward and then southward off the coast of Cabo Delgado.

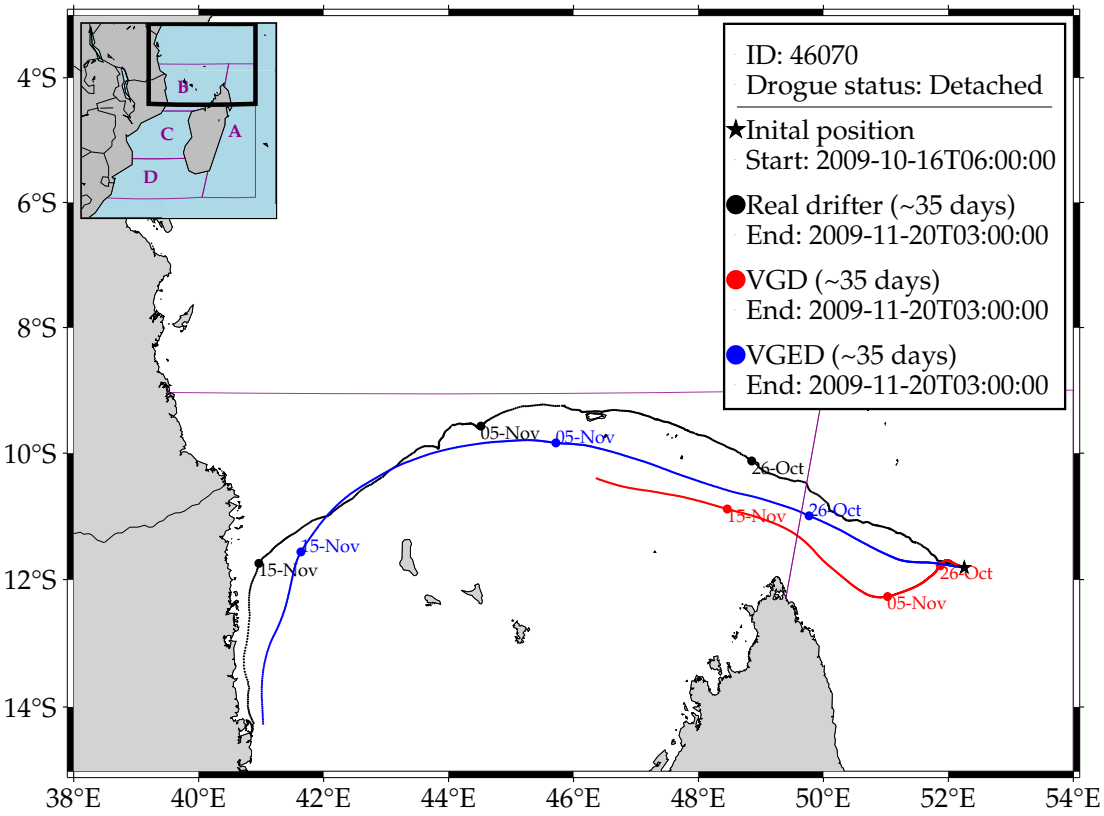

Figure 4.2: *Trajectories of real drifter 46070 and virtual drifters (VGD - red and VGED - blue) over 35 days. The real drifter travelled from 16 October 2009 to 20 November 2009 with a detached drogue before entering the domain.*

The virtual drifters follow different tracks from the real drifter despite starting from the same initial position.

The VGD takes a track that diverges slightly from the real drifter's trajectory but shows a tendency to move westward. However, the VGED exhibits a quasi-similar path with the real drifter. Although the VGED travels a shorter distance than the real drifter in the first 10 days, the trajectory was almost identical to the real drifter. In contrast, VGD reached the integration time, travelling approximately ∼25 km in the first 10 days, while VGED ∼200 km and real drifter ∼300 km.

Figure 4.3 depict the trajectories of real and virtual drifters 62575 over 43 days. The real drifter travelled between December 20 2009, and February 1 2010. The real drifter drogue was detached inside the CMC (marked with an **x** on the map) 5 days after its deployment. From that day on, the real drifter became susceptible to wind and surface effects. The real drifter covers a considerable area, initially moving southward, then northward, then shifting westward, and finally southwestward. These meandering patterns indicate the influence of mesoscale eddies, as this drifter was intentionally deployed on the edge of an eddy. The estimated eddy diameter in this figure was ∼100 km from the first loop and increased to ∼200 km in the loop of January 9 2010. However, the VGD also follows a northward trajectory, but the track remains more constrained, lacking the extensive meandering observed in the real drifter.

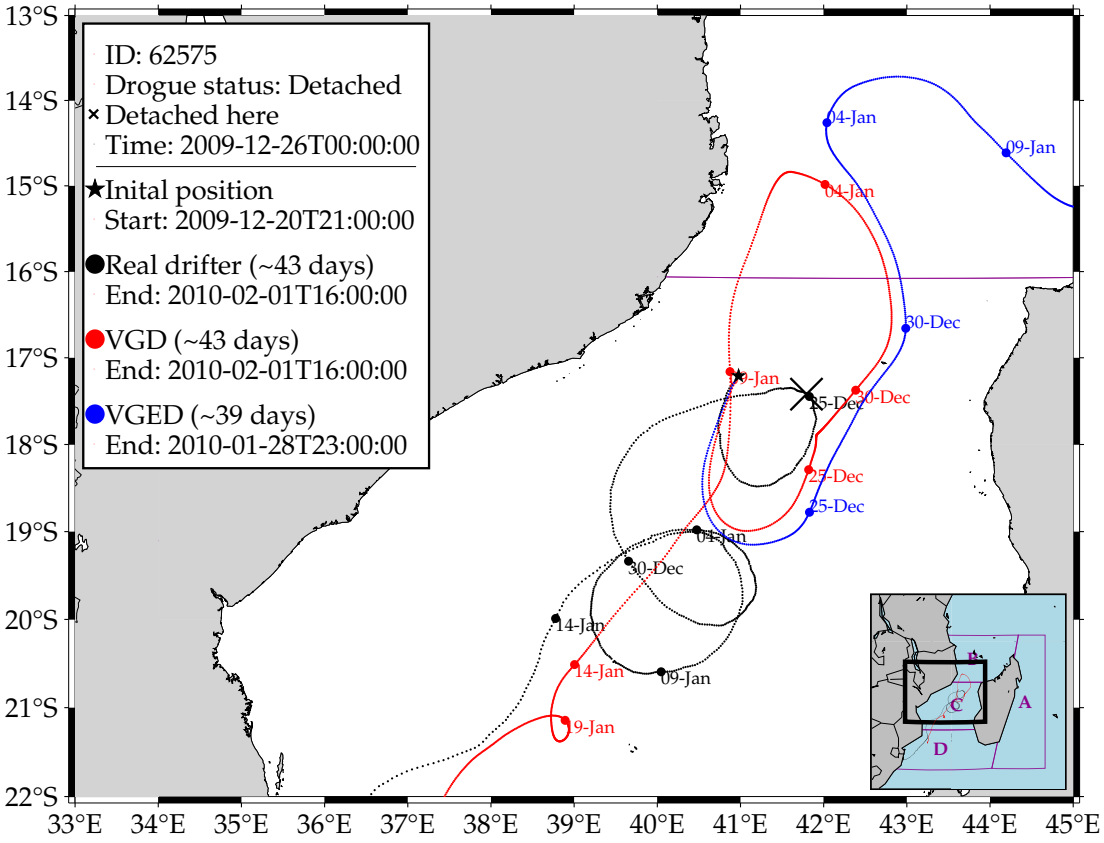

Figure 4.3: *Trajectories of real drifter ID: 62575 and virtual drifters over a 43-day period. The real drifter travelled from 20 December 2009 to 1 February 2010 with a detached drogue.*

The VGD path stays closer to VGED and does not exhibit the same level of interaction as the real drifter.

The device eventually travelled southward after January 4 2010, and fast enough to stay in almost the same position as the real drifter on January 14 2010. After 5 days from January 14 2010, the VGD made a loop with a mean diameter of approximately ∼27 km. Nonetheless, the VGED had a trajectory almost similar to VGD until January 4 2010, where a strange behaviour occurred for 10 days with limited movement. The virtual drifter eventually travelled east and south to the coast of Madagascar, ultimately running aground and failing to complete the integration time.

Figure 4.4 highlights the trajectories of a real drifter 17442 and two virtual counterparts over 35 days. The real drifter travelled from March 28 2000 to May 2 2000, with the drogue still attached. The drifter's track was mostly southward, with some meandering, suggesting a steady interaction with an eddy moving southward. The figure shows that the real drifter travels quickly, completing two loops in the first 10 days.

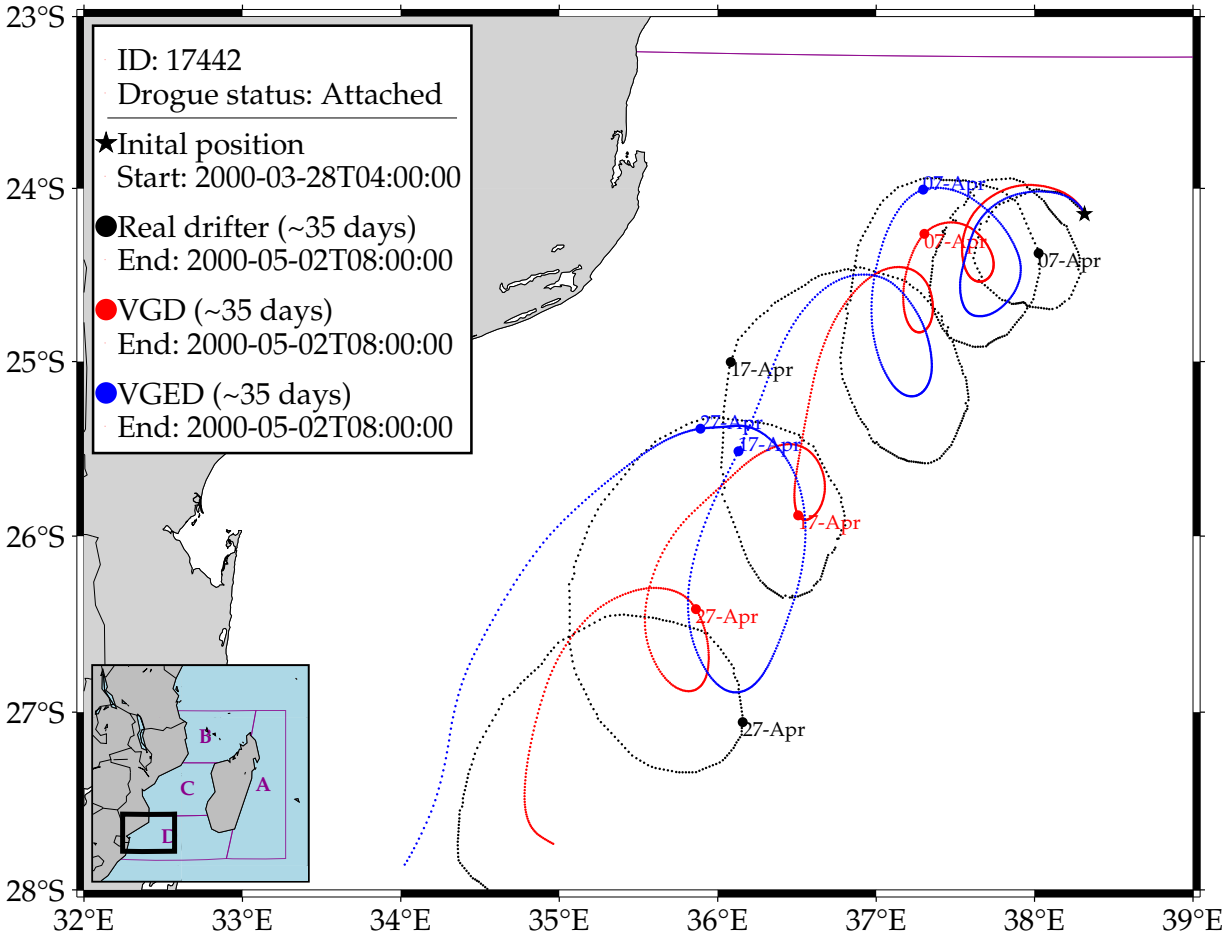

Figure 4.4: *Trajectories of real drifter (ID: 17442) and two virtual drifters over 35 days. The real drifter travelled from 28 March 2000 to 2 May 2000 with the drogue attached, following subsurface currents.*

The VGD shows a track that generally follows a southward trajectory similar to the real drifter but was more constrained regarding deviation and meandering. However, VGED follows a path similar to VGD but shows slightly more variation in its track. Despite this, the VGED still underestimates the real drifter's movement

and remains more confined than the real drifter's broader meandering path. The real drifter shows a more complex and varied trajectory, while both virtual drifters exhibit more constrained paths. The presence of the drogue for the real drifter indicates subsurface currents influenced the movement. In contrast, the virtual drifters do not capture the full extent of the real drifter movement.

4.1 Drifters interaction with moving eddy

The trajectory illustrated through the real drifter and virtual counterparts reveals the complex interactions between geostrophic and Ekman dynamics, represented across various stages in *Figure 4.5*. Significant variations in loop formation, mean diameters, and velocity provide a deeper understanding of these processes. The ERS-2 satellite orbit shows a 0.3 m sea level anomaly (SLA) where the drifter was deployed, which means the device was deployed on an anticyclonic eddy, while a -0.3 m SLA was on the west side, close to the coast.

In *Figure 4.5(a)* initially, the real drifter follows a compact path over the course of approximately 5 days, forming a loop with a mean diameter of ∼68 km over 4 days. The VGD shows a smaller, more constrained loop of ∼26 km over 5 days. The VGD trajectory lacks the lateral influence experienced by the real drifter. In contrast, the VGED produces a larger loop of ∼52 km over 7 days. The broader path of the VGED highlights the role of Ekman drift in amplifying the lateral displacement compared to the VGD, though the full extent of the real drifter was not reached.

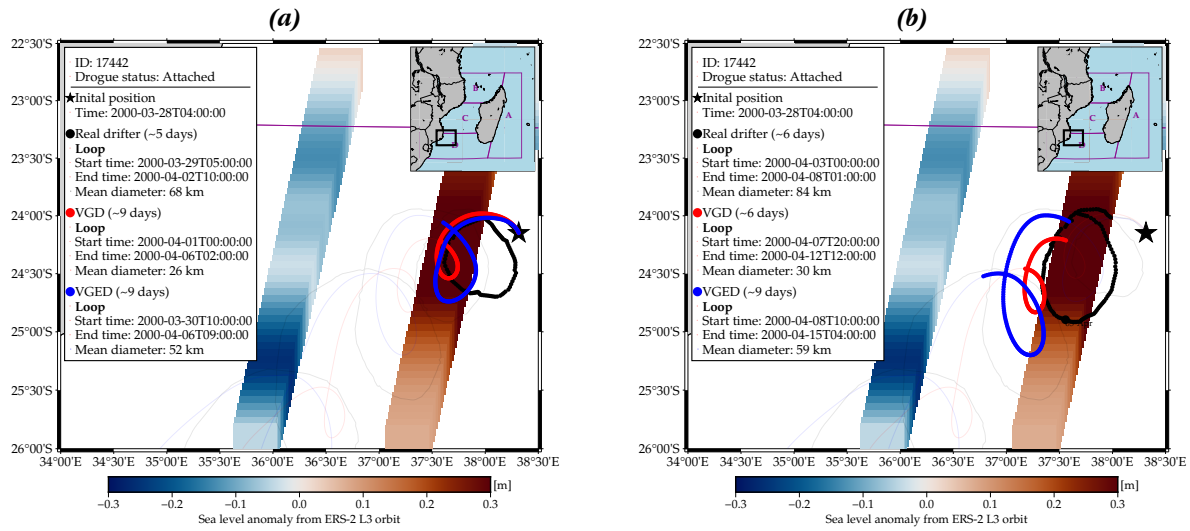

Figure 4.5: *Trajectories of the real and virtual drifter (ID: 17442) across distinct stages. (a) and (b) panels show the progression of the drifter over time, with key differences in loop size and displacement highlighted by their mean diameters. The sea level L3 orbit from ERS-2 satellite, correspond to the period of 2000-03-29T07:38:29 to 2000-04-04T20:10:56 acquired from European Union-Copernicus Marine Service (2021).*

In *Figure 4.5(b)*, the second stage shows that the real drifter forms another larger loop with a mean diameter of 84 km over 5 days. The VGD, in this case, traces a smaller loop with a mean diameter of 30 km over 5 days, continuing to show the limited influence of geostrophic-only currents. Meanwhile, the VGED covers a broader area with a loop diameter of 59 km over 7 days, indicating that wind-driven forces are again playing a substantial role in widening the trajectory. However, the VGED falls short of the extent of the real drifter.

The velocity in *Figure 4.6* offers a key understanding of the drifter's movement through time. The first solid

line for the real drifter aligns with the first loop in *Figure 4.5(a)*, showing an increase in velocity during the 4-day circular trajectory period as the drifter interacts with the eddy. This velocity spike indicates the drifter's acceleration while entrained in the mesoscale feature. The second solid line corresponds to the second loop in *Figure 4.5(b)*, where the real drifter experiences another peak in velocity, initially relatively slow, and progressively reaches a higher velocity this time while moving out of the loop.

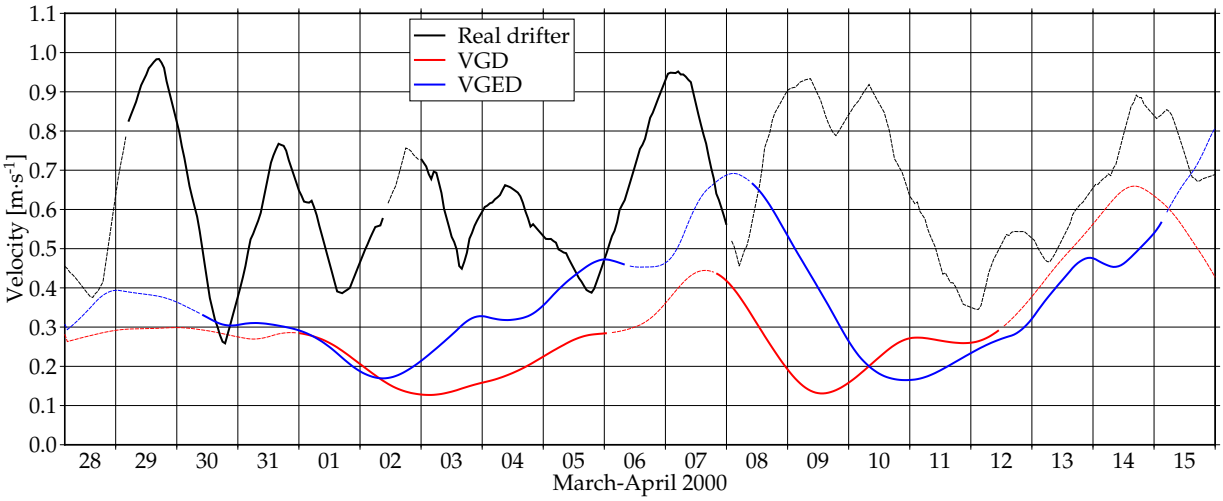

***Figure** 4.6: Velocity time development of the real and virtual drifters (ID: 17442) across distinct stages. This represents the velocity during the progression in Figure 4.5; the solid lines are the velocity during the loops.*

For both the VGD and VGED, the velocity time development displays distinct patterns that align with the formation of loops. While both virtual drifters exhibit lower velocities than the real drifter, the VGED shows slightly higher velocities than the VGD, a reflection of the additional influence from Ekman drift. Interestingly, the peaks in velocity occur during transitional phases rather than within the loops themselves, as indicated by the solid lines marking the looping periods. The higher velocities are more likely to be linked to the drifters entering or exiting the looping phase. The velocity of both virtual drifters was always slow in mid-trajectory.

In contrast to expectations, the velocity spikes in both virtual drifters do not coincide with the periods when the drifters are fully engaged in the looping motion. Instead, these peaks occur when the drifter transitions between straight-line movement and the loop, particularly for the VGED. This behaviour highlights that while steady geostrophic currents drive the loops themselves, the changes in velocity are influenced more by the interaction between the drifters and surrounding forces as they transition into and out of these loops.

Since they tended to follow the eddy, the average centroid southward velocity of real drifter, VGD and VGED was 8.8, 12, and 11.3 km day^{-1}, respectively.

Analysing movement of a different drifter in the SMC *Figure 4.7*; the figure also captures the drifter's progression across distinct stages, with key differences in loop formation, mean diameters, and velocities.

In the first phase, *Figure 4.7(a)* shows that the real drifter moves over approximately 10 days, forming a

large loop with a mean diameter of 99 km. This expansive loop suggests the drifter interacts with a robust mesoscale eddy, which drives the substantial displacement. As observed in the sea level anomaly data from the Jason-1 satellite orbit, the drifter was deployed within a cyclonic eddy exhibiting westward movement. The VGD follows closely, forming a loop of 98 km over the same 7-day period, indicating that geostrophic-only currents are sufficient to replicate much of the real drifter's path. However, the VGED forms a slightly smaller loop with a mean diameter of 78 km over 9 days. This suggests that the influence of Ekman drift, while present, does not significantly broaden the drifter's path during this stage.

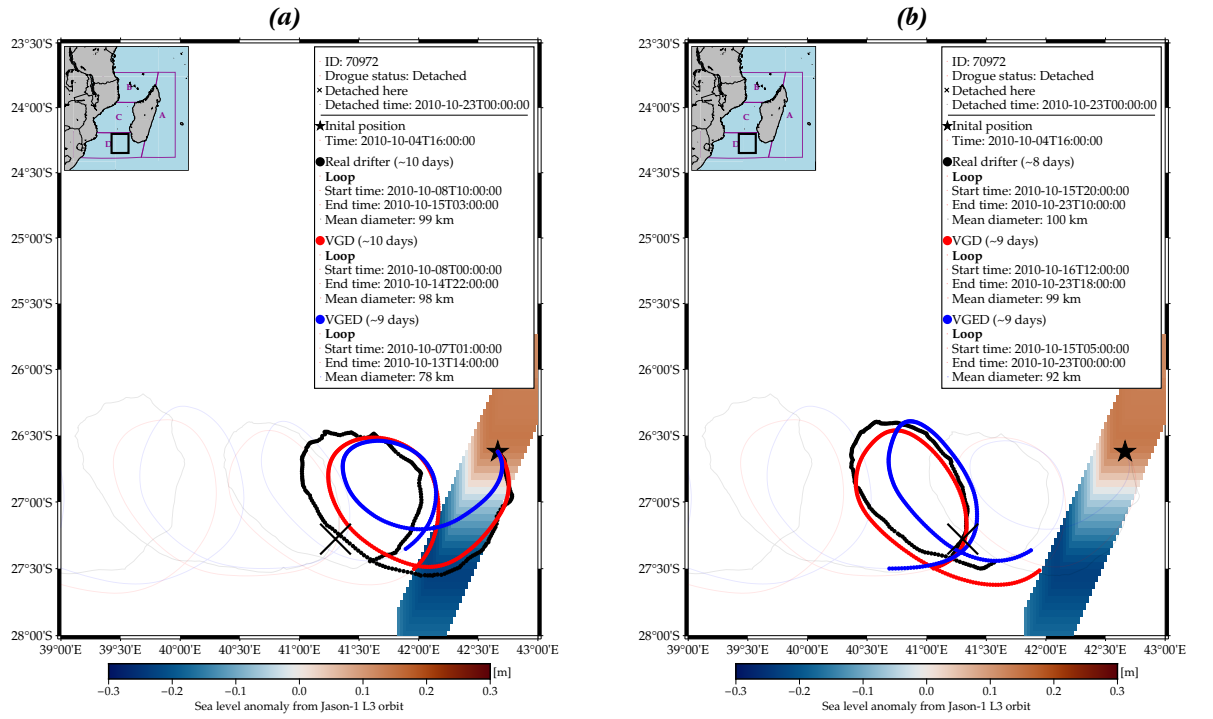

Figure 4.7: *Trajectories of the real and virtual drifter (ID: 70972) across distinct stages. (a) and (b) panels show the progression of the drifter over time, with key differences in loop size and displacement highlighted by their mean diameters. The sea level L3 orbit from Jason-1 satellite corresponds to the period of 2010-10-04T16:00:00 to 2010-10-10T14:00:00 acquired from European Union-Copernicus Marine Service (2021).*

In the second stage, the real drifter continues the trajectory, forming another loop with a mean diameter of 100 km over 8 days *Figure 4.7(b)*, with an average centroid velocity of 9.5 km day^{-1}. This loop, marginally larger than the first, suggests that the drifter remains under the influence of a strong mesoscale eddy. The VGD traces a near-identical path, forming a loop with a diameter of 99 km over 9 days and a centroid velocity of 13.8 km day^{-1}, reinforcing the importance of geostrophic currents in driving the drifter's motion. The VGED, however, forms a slightly stretched loop with a mean diameter of 92 km over 9 days with an average centroid velocity of 12.7 km day^{-1}, reflecting a more pronounced influence of Ekman drift in this stage. The minor increase in loop size for the VGED suggests that wind-driven forces are starting to play a more significant role in widening its trajectory compared to the VGD. During the second loop, the drifter lost the

drogue but did not suffer much deviation, as all the tracks were aligned (shaded lines represent the rest of the tracks).

The velocity in *Figure 4.8* further illustrates the drifter's behaviour through time. The first solid line for the real drifter aligns with the looping period from October 8 to 15 2010, during which the velocity decreases in the first 2 days inside the loop and slightly increments with variation until October 15. The second solid line marks the period from October 15 to 23 2010, where the drifter experiences another velocity peak, corresponding to the formation of the second loop, decreasing the velocity in the 3 days and increasing with slight variation until October 23. Interestingly, these velocity spikes occur when the drifter transitions into or out of the loops.

For the VGD and VGED, their velocities display a similar pattern, with slightly lower velocities compared to the real drifter. The velocity peaks in both virtual drifters occur during their respective looping phases but at reduced magnitudes. The VGED shows a slight increase in velocity at some stages compared to the VGD, reflecting the added contribution of Ekman drift. However, the general behaviour remains consistent, with velocity increases occurring during transitions into or out of loops. The small differences in velocity between the two virtual drifters indicate that Ekman drift plays a modest role in accelerating the VGED during these transitions.

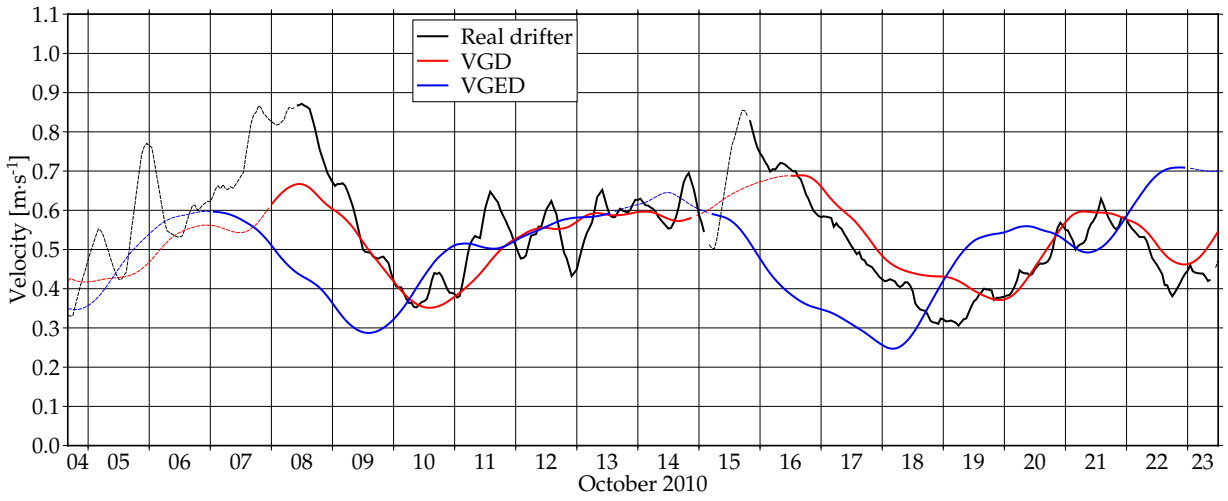

Figure 4.8: *Velocity time development of the real and virtual drifters (ID: 70972) across distinct stages. This represents the velocity during the progression in Figure 4.7; the solid lines are the velocity during the loops.*

4.2 CNES-CLS18 performance

The data presented in *Table 4.1* illustrates the percentage underestimations of surface velocities by geostrophic-only and geostrophic + Ekman currents in comparison to real currents in four different regions: the East Madagascar Coast (EMC), Northern Mozambique Channel (NMC), Central Mozambique Channel (CMC), and Southern Mozambique Channel (SMC).

In the geostrophic-only velocity field, the EMC displays the highest underestimation at 47%, followed by the SMC at 33%. The CMC and NMC exhibit lower underestimations of 18%. The total average underestimation for all regions by geostrophic-only currents was 29%. Furthermore, the virtual drifters accounted for 86% of the total integration time from the real drifter data. This indicates that, although the geostrophic-only currents successfully capture most drifters, the velocities tend to be underestimated with some virtual drifters going ashore.

Table 4.1: *Percentage of velocity underestimation for geostrophic and geostrophic plus Ekman currents compared to real drifters in different regions of the domain (refer to Figure 3.1). The integration time column represents the percentage of total time steps from the real drifter data covered by the virtual drifters. The integration time percentage reflects the extent to which the virtual drifters either ran aground or left the velocity field's domain. Inside brackets, there are a number of drifters by region and velocity fields.*

Velocity field	Regions					Integration time
	EMC	NMC	CMC	SMC	Average	
Geostrophic-only	47%(131)	18%(89)	18%(8)	33%(13)	29%	86%
Geostrophic + Ekman	22%(131)	20%(92)	18%(8)	24%(14)	21%	75%

The geostrophic + Ekman velocity field shows a noticeable reduction in underestimation, particularly in the EMC and SMC, where the percentage drops to 22% and 24% respectively, compared to geostrophic-only. In contrast, underestimation in the NMC increased to 20%, and stayed the same in the CMC. The overall average underestimation across all regions by the geostrophic + Ekman velocity field was 21%, which shows enhanced accuracy compared to the solely geostrophic velocity field, although the difference was marginal. Notably, the underestimation was accompanied by a reduction of 11% of the total integration time of the purely geostrophic.

4.3 Drifter dispersion released within an area in the Northern Offshore of Cabo Delgado

Virtual drifters were released inside Area 4 in the northern offshore of Cabo Delgado (*Figure 4.9*(a)), where Mozambique's major Floating Liquified Natural Gas (FLNG) facility was exploring natural gas. The virtual drifters were released to analyse the dispersion of possible debris in case of accidents. *Figure 4.9*(b) shows the 20-year monthly means (2000 - 2019) of distance travelled by the 480 virtual drifters. The map trajectory linked to this figure was presented in Appendix D in *Figure D.1*. The virtual drifters were deployed randomly inside Area 4 and divided into 40 monthly virtual drifters over 20 years (20 each for VGD and VGED). The integration time was the total number of days of the respective simulation months, precisely 28 to 31 days.

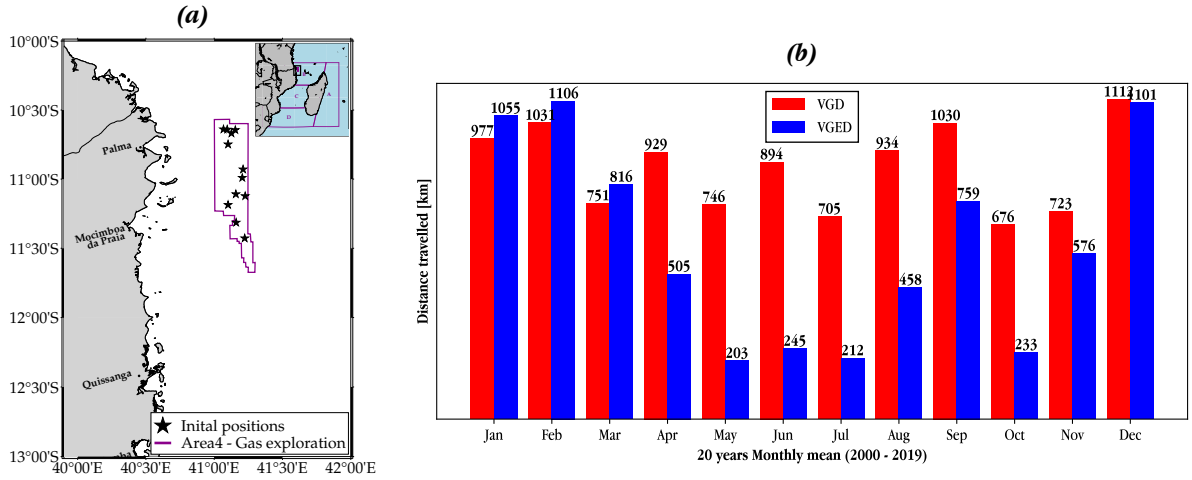

Figure 4.9: *(a) Location of Area 4 in the Northern Offshore of Cabo Delgado. The stars represent the virtual drifter's initial positions determined randomly inside the Area 4 polygon. They were set to run for the entire month, with a time step of 1 hour. The geostrophic-only and geostrophic+Ekman velocity fields were used to calculate the trajectories. The overlap trajectories of these virtual drifters can be found in the Appendix D in Figure D.1. (b) Monthly mean distance travelled by 480 virtual drifters between 2000 and 2019.*

In *Figure 4.9*(b), VGED travelled significantly shorter distances, below 460 km, in May, June, July and August, which are assumed to be winter. This indicates that the VGED immediately ran aground. In September, October, and November, the distance gradually varied from 759 to 233 km in the transition season from winter to summer. Assuming December, January and February are summer months, the distances covered for VGED are above 1000 km, which indicates that the virtual drifter travels longer than in winter season. Finally, in the transition from summer to winter (March, April and May), the distances covered by VGED gradually decreased, ranging from 816 to 203 km.

The distances from VGD varied between 676 to 1112 km, which indicates they travel longer than overall VGED. When comparing VGD with VGED, evidence shows that seasonality plays a significant role on VGED dispersion.

Chapter 5: DISCUSSION

In the EMC represented in *Figure 4.1*, the trajectories of the drifters 40551 define well the direction of the SEMC. Since geostrophic currents are major contributors to surface circulation (Rio et al., 2014), the SEMC was a southward continuation of SEC, and was a result of increased sea surface level near the coast (Voldsund et al., 2017). This elevated area creates a slope leading down to the coast, producing a southward geostrophic flow. In fact, after SEMC moves away from the Madagascar coast, it flows southwest and disperses into a consistent pattern of symmetrical counter-rotating eddy pairs (Ridderinkhof et al., 2013). This current behaviour was not well described by any of the drifters, as the frequency of the counter-rotating eddy pairs was 4-6 per year (Ridderinkhof et al., 2013). Taking a closer look at the real drifter, after March 18, the device deviates west and north into CMC, rather than southwest. The drogue status and local winds explain this behaviour. In March, the southern tip of Madagascar experiences easterly winds (Emílio, 2020; Halo & Raj, 2020). This might explain the real drifter deviation, as this drifter had no drogue attached, which made the device susceptible to wind-driven slip. Although wind-driven slip was the main factor due to the absence of drogue, various ageostrophic currents linked to internal oscillations, tidal currents, Stokes drift, and internal ocean dynamics also comprise the real drifter's current (Menna et al., 2018).

As for the virtual drifters, they represented the trajectory well along the coast of Madagascar relative to the real drifter. The position in time shows a prolonged current with VGD the slowest one. However, the counter-rotating eddy pairs by Ridderinkhof et al. (2013) were later analysed by Vianello et al. (2020), where there was an indication that the dipole had a strong interaction with the irregular bathymetry, defined by a cluster of five seamounts located between 240 and 1200 m depths. Additionally, the bathymetry blocked the dipole's westward movement, confining it near the seamount for over four weeks. Based on the results by Vianello et al. (2020), assuming this behaviour of the dipole in the southern tip of Madagascar was responsible for the VGD to continue southeastward was logical.

In contrast, the VGED travelled to SMC as the virtual drifter has the Ekman drift component. Although SEC and Ekman drift in the east of Madagascar are weak (Ma et al., 2021), the Ekman drift was evident in the south. As winds are easterly in the southern tip of Madagascar, by integrating and solving *Equation 2.4*, the result was the u_E and v_E components having the same magnitude. This means that the surface drift due to Ekman was 45° to the left of the direction of the winds (Mulet et al., 2021), which was evident after March 28 2008, although later started to shift north.

Even though drifter 46070 (*Figure 4.2*) started in the EMC, the real drifter spent most of the journey in NMC. This drifter follows another continuation of SEC to the north of Madagascar coast, the Northward East

Madagascar Current (NEMC), and this current splits around 12° S creating a branch to the north (Halo & Raj, 2020; Voldsund et al., 2017) and another to the south highlighted by the drifter 46070. The real drifter and VGED demonstrate wind influence in this region, and the VGD cannot take advantage. The real drifter had no drogue attached; hence, the device immediately went aground due to interaction with instant winds and waves. The VGED followed almost the same path, while the VGD stopped earlier due to slow velocity. When assessing the influence of wind-driven Ekman currents in the Channel, currents are predominant during the peak of the monsoon in the northern region of the Channel and the passage of atmospheric cyclones (Ternon et al., 2014b). Interestingly, during the final days of this drifter, the moderate Tropical Storm Bongani was being formed (*Figure C.2*). This tropical cyclone only caused the drifters affected by wind dynamics to follow the same path. The real drifter strictly followed this path due to the intense winds from the tropical storm, having lost the drogue and become susceptible to the winds. Although arguing the same for VGED was not possible, the similar path of this virtual drifter might be related to winds disrupting the classic Ekman spiral structure, which results in a more uniform flow direction closer to the wind.

In the CMC (*Figure 4.3*), the real drifter, having lost the drogue after 5 days, exhibited extensive meandering and covered a considerable area, influenced by wind and mesoscale eddies. In contrast, the VGD followed a more constrained path, lacking the complex deviations observed in the real drifter, indicating an underrepresentation of mesoscale variability. Interestingly, even with the drogue detached, assumptions were made that the drifter did not prevail under instantaneous winds and waves, as this region, especially during summer, registers moderate winds (Emílio, 2020). Meanwhile, the VGED showed even more limited movement over a shorter 15-day period, suggesting that the addition of Ekman velocities does not adequately capture the dynamic circulation in this region. Similarly, mesoscale eddies significantly influence drifter trajectories in the CMC. Observations indicated that drifters were moving through frontal zones between eddies, avoiding entrapment within them (Hancke et al., 2014). This was commonly observed among SVP drifters deployed outside eddies on the study by Hancke et al. (2014) and was observed in *Figure 4.3* by virtual drifters. These virtual drifters followed the eddy boundary. Later, instead of following the real drifter to the southwest, the virtual drifters moved out of the eddy and continued North, showing interaction with frontal zones between eddies.

The central part of the Channel was the second-most energetic in the entire WIO region after the eastern extension of the Agulhas Return Current (Halo & Raj, 2020). As the region appeared to be a site favouring anticyclonic eddy formation (Halo et al., 2014), similar mean diameters as the ones from Halo et al. (2014) were also found. Moreover, seasonality affects around 20% of eddy kinematic energy, which was considered relatively insignificant (Halo & Raj, 2020).

To comprehend the intricate dynamics of CMC, a reset of the initial position and simulation for virtual drifters was presented after 5 to 10 days (*Figure 5.1*). In the *Figure 5.1(a)* after resetting the initial position of virtual

drifters, the trajectory was close to the real drifter. The chosen initial position was where the real drifter lost the drogue. After 5 days, on December 31, 2009, all the drifters were almost at the exact location, and the track was similar. This outcome indicates that, despite the real drifter losing the drogue, it did not experience wind-driven slippage. Hence, the virtual drifters, which always lacked the drogue component, followed the same path. This also proves that, with or without a drogue, the drifter's interaction with mesoscale features demonstrates the energetic nature of this region.

In the *Figure 5.1(b)* after resetting the initial position of virtual drifters, as were deployed on the last position of the real drifter in *Figure 5.1(a)*, the track was similar to the real drifter in the first 5 days. However, 5 days after January 10 2010, the virtual drifters moved out of the eddy, highlighting this region's complexity. An argument could be made for the interaction of virtual drifters with a cyclonic eddy, as these eddies originate mainly along the eastern boundary of the Channel (Halo et al., 2014). This argument reinforces the observation by Hancke et al. (2014) that SVP drifters navigate between frontal eddies, although, in this case, observations show movement by virtual drifters. Another important aspect was that an eddy's ability to retain the structure and trap particles within its core was associated with nonlinearity due to rotational speed exceeding its translation speed (Chelton et al., 2011). Halo and Raj (2020) also evaluated the eddy rotational speed and nonlinearity and observed that in the CMC, cyclonic eddies were strongly more nonlinear than the anticyclonic. Since the primary eddy in *Figure 5.1* was anticyclonic, connecting the virtual drifters exiting the eddy with linearity behaviour was logical. This shows that the eddy in real velocity field was nonlinear, and the CNES-CLS18-derived velocity fields were linear in this region.

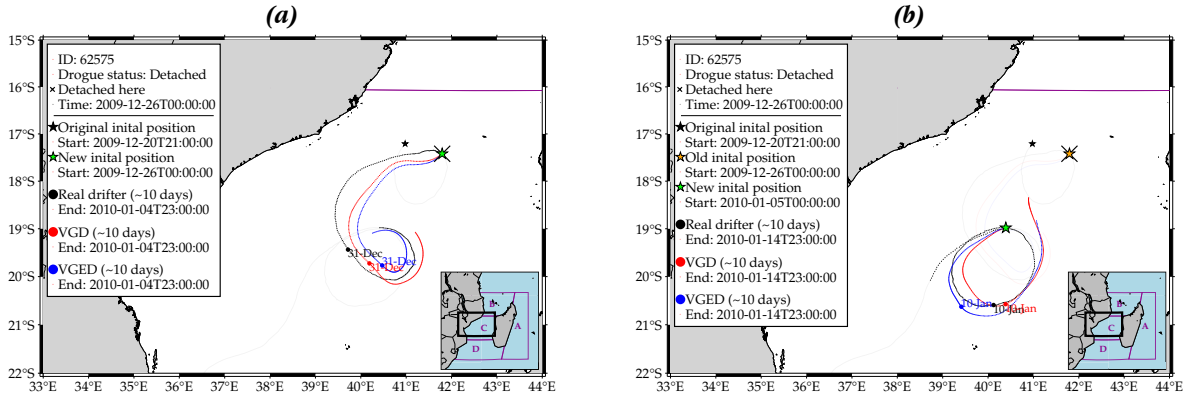

Figure 5.1: *Trajectories of the real and virtual drifter (ID: 62575) across distinct stages. (a) and (b) panels show the progression of the drifter over time.*

In the SMC, the trajectory of real drifter 17442 (*Figure 4.4*), observed over 35 days with the drogue attached, showcases intricate southward movement within an eddy. This complex path reflects the strong influence of mesoscale eddies prevalent in this region, which are known to drive significant southward transport (Roberts et al., 2014). In contrast, both virtual drifters exhibit more constrained trajectories, lacking the extensive me-

andering displayed by the real drifter. Despite including Ekman dynamics, the VGED still underestimates the drifter's movement, indicating that the models do not fully capture the eddy-induced variability (Swart et al., 2010). This discrepancy highlights the limitations of the virtual models in representing the dynamic circulation patterns associated with mesoscale eddies in the SMC, especially the moving ones. Another perspective suggests that these virtual velocity fields lack the resolution to capture mesoscale features fully. Following the previous discussion about the nonlinearity of anticyclone eddies, the drifter 17442 seems to exhibit strong nonlinearity; hence, the trajectories of all drifters appear tightly bound to the southward eddy.

The *Figure 5.2* compares the instantaneous velocity and displacement distributions across four discussed drifters. The real drifters are represented in grey, while the virtual drifters, both VGD and VGED, are shown in colours. Each section of the figure corresponds to a specific drifter ID (40551, 46070, 62575 and 17442).

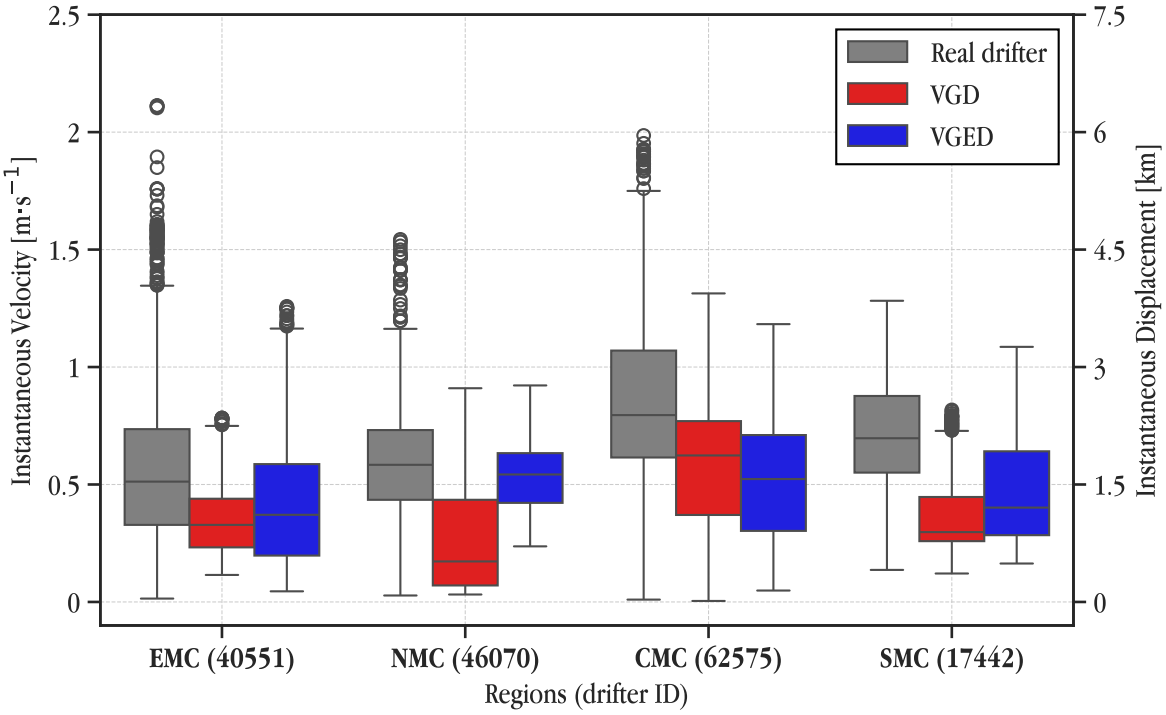

Figure 5.2: *Comparing velocity (left panel) and instantaneous displacement (right panel) distributions for real drifters and virtual drifters across four regions of the domain. IDs 40551, 46070, 62757, 17442 are within EMC, NMC, CMC and SMC regions, respectively. The boxes indicate the Interquartile Range (IQR), with a line inside each box showing the median value. Vertical bars, known as whiskers, extend to encompass the data range up to 1.5 times the IQR, while circles represent outliers that lie beyond this range.*

Analyzing the instantaneous velocity and displacement of all four above drifters in *Figure 5.2* regarding *Figure 4.1* to *Figure 4.4*, observations revealed that:

- Real drifters across all regions have high instantaneous velocity and, as indicated by the wider Interquartile Ranges (IQR) and higher medians. This observation was explained by $u_{dr} = u_g + u_e +$

$u_s + u_a$, where u_{dr} was the current real drifter measure. There was a sum of various contributions, including u_g (geostrophic currents), u_e (Ekman currents), u_s (wind-driven slippage) and u_a (ageostrophic currents), which was associated with the internal oscillations, tide currents, Stokes drift, internal ocean dynamics (Menna et al., 2018). A consequence of high instantaneous velocity means a high instantaneous displacement.

- VGD has slightly high instantaneous velocity IQR in the CMC, which shows this region strong geostrophic-only dynamics. Although summing with Ekman drift should increase the velocity, the VGED demonstrate that Ekman introduced more variability and complexity (Hart-Davis et al., 2018) in this region, although the difference was marginal. Other regions have high instantaneous velocity IQR, which shows winds have more direct effects on drifter's movement.
- Interestingly, the IQR are higher in CMC compared to the rest, reinforcing the region's energetic aspect in driving drifters.

5.1 Drifter within a moving eddy

The observed trajectories of drifter *ID: 17442* (*Figure 4.5*) and the virtual counterparts illuminate the intricate interplay between geostrophic currents and wind-driven Ekman dynamics in the SMC. The real drifter, with the drogue attached, demonstrates substantial looping patterns with mean diameters of 68 and 84 km over successive periods, indicative of strong interactions with mesoscale eddies (Cossa et al., 2016; Halo et al., 2014).

The interaction of these drifters with the moving southward eddy shows interesting dynamics. A regional ocean model shows circulation in the Delagoa Bight (between 25 - 27° S and 31 - 35° E), where a semi-permanent cyclonic eddy, the Delagoa Bight Lee Eddy (DBLE) occurring about 25% of the time (Cossa et al., 2016). The formation of this eddy was discovered to be a result of the shedding of nearshore waters, as the nearshore flow intensifies due to an anticyclonic eddy around 24° S. The drifters were deployed in the anticyclonic eddy, much further off the coast, suggesting that the interaction between these two features resulted in a more confined loop in the VGD.

The velocity-time developments further elucidate these dynamics (*Figure 4.6*). The real drifter exhibits velocity peaks during looping periods, aligning with the acceleration expected when entrained within a mesoscale eddy. This behaviour contrasts with the virtual drifters, where velocity spikes occur during transitional phases rather than within the loops. The VGED shows slightly higher velocities than the VGD, reflecting the additional influence of Ekman transport. Yet, both remained lower than the real drifter's velocities. This discrepancy suggests that the virtual drifters inadequately capture the acceleration associated with eddy entrainment, possibly due to insufficient resolution for capturing mesoscale less than 100 km in diameter and submesoscale features (Hancke et al., 2014).

The average southward velocity of the centroid drifters highlights an unexpected overestimation by the virtual models (*Figure 4.5*). This average southward velocity was calculated by the difference in the centroid distance and time from *Figure 4.6(a)* and *Figure 4.6(b)*. The overestimation may be attributed to the model's inability to accurately simulate the complex vorticity and shear associated with mesoscale eddies, leading to discrepancies in drift speed and direction (Backeberg & Reason, 2010). Moreover, the significant role of wind-driven currents, particularly during strong wind events or atmospheric cyclones, can induce ageostrophic motions that are challenging to represent in numerical models (Ternon et al., 2014b). Surprisingly or not, the winds from Tropical Cyclone HUDAH (*Figure C.1*) did not affect the movement of the real and virtual drifters, although the HUDAH's landfall was central to the North coast of Mozambique. As was evident from the drogue status, this drifter had the drogue attached.

Moving further southeast of the Channel drifter *ID: 70972* in *Figure 4.7* in the first phase forms a large loop with a mean diameter of 99 km over approximately 10 days, indicating strong interaction with mesoscale

cyclonic eddy. Sea level anomaly data from the Jason-1 satellite confirm the presence of a westward-moving cyclonic eddy at the drifter's deployment location.

The VGD closely mirrors the real drifter's path during this phase, forming a loop of 98 km over 7 days. This suggests that geostrophic dynamics predominantly govern the drifter's movement in this instance (Backeberg et al., 2008). The VGED forms a slightly smaller loop with a mean diameter of 78 km over 9 days. The reduced loop size implies that wind-driven Ekman transport does not significantly influence the trajectory during this stage. This was evident in the wind fields by Halo and Raj (2020), where the intensity during this period was low.

In the second phase, the real drifter traces a loop with a mean diameter of 100 km over 8 days, maintaining the interaction with a robust mesoscale eddy. Despite losing the drogue during this period, the drifter's path remains largely unaffected, suggesting the eddy's strong influence overrides the loss of subsurface tracking capability. This reinforces the observation by Halo and Raj (2020), where cyclonic eddies in the SMC are more nonlinear than anticyclonic, which results in the retention of the particles within the eddies.

The velocity time development in *Figure 4.8* further elucidate these dynamics. For the real drifter, velocity spikes occur during transitions into and out of the looping phases, suggesting accelerations are associated with interactions at the eddy boundaries rather than within the eddy core (Hancke et al., 2014).

5.2 Velocity field performance

The performance of the velocity fields derived from CNES-CLS18 in *Table 4.1* highlights significant underestimations in surface velocity measurements when relying solely on geostrophic currents, particularly in the EMC and SMC, with underestimations higher than 30%. Examining *Figure 5.3*, higher velocities are evident for VGED in the EMC and SMC, as winds are more pronounced in these regions. On the southeast coast of Madagascar, sometimes winds are southward along the coast, promoting upwelling and increasing downstream toward the southeast corner of Madagascar (Voldsund et al., 2017).

In the NMC, underestimation was the lowest except for a marginal increase of 2% for VGED. This increase might be negligible, as in the *Figure 5.3* the velocity was high for VGED. An additional argument suggests that VGED velocities in this region may vary seasonally, whereas VGD remains unaffected by seasonal changes. This might explain why there was high velocity resulting in 20% underestimation for VGED and low velocity followed by 18% underestimation for VGD. In the western boundary of NMC, the velocities are significantly higher, showing a prevalence of western boundary current along the coast of Cabo Delgado (Ullgren et al., 2016).

The CMC shows the exact value of underestimations for both velocity fields, and being the lowest, this explains that Ekman drifts change the course of a drifter but do not affect the velocity. This fact underscores the significant role of wind-driven Ekman dynamics in the surface circulation of the region, as also observed in another study, which emphasised that wind-induced coastal upwelling, driven by alongshore winds, was a crucial mechanism influencing surface currents and enhancing chlorophyll-a concentrations in the region (Malauene et al., 2014). A part of this coastal upwelling was also linked to mesoscale eddies, and it was also evident from *Figure 5.3* that VGD capture well the mesoscale features with relatively high velocity.

Overall, the underestimations are lower than 30%, which was less than the 35% reported by Hart-Davis et al. (2018) in MC. This fact highlights the improvement of CNES-CLS18 derived velocity field compared to CNES-CLS13 used by Hart-Davis et al. (2018).

Despite the reduction in velocity underestimation, the incorporation of Ekman drift results in most virtual drifters running ashore, decreasing the integration time from 86% coverage with geostrophic-only currents to 75% with the addition of Ekman dynamics. This limitation may be due to the increased variability and transient nature of wind-driven currents, which are challenging to model accurately over extended periods (Hart-Davis et al., 2018). Additionally, uncertainties in the Ekman currents arise from improper knowledge of mixed layer depths and their variability in such a dynamic regime (Hart-Davis et al., 2018), affecting the model's ability to replicate real drifter trajectories consistently.

The disparities between the real and virtual drifter data underscore the critical role of mesoscale eddies and boundary currents in shaping the Mozambique Channel's dynamics. Studies have shown that anticyclonic

eddies, occurring at a frequency of four to seven per year, dominate the flow within the Channel, significantly impacting transport and hydrographic variability (Schouten et al., 2003; Ullgren et al., 2012).

Moreover, the real drifter data's comprehensive coverage and detailed depiction of the EMC, NMC, CMC, and SMC highlight the importance of in-situ measurements for understanding the Mozambique Channel's circulation. The challenges in accurately modelling such a dynamic and complex region are evident, emphasising the necessity for continuous observational data to validate and improve numerical models (Backeberg et al., 2008; Hancke et al., 2014; Hart-Davis & Backeberg, 2021).

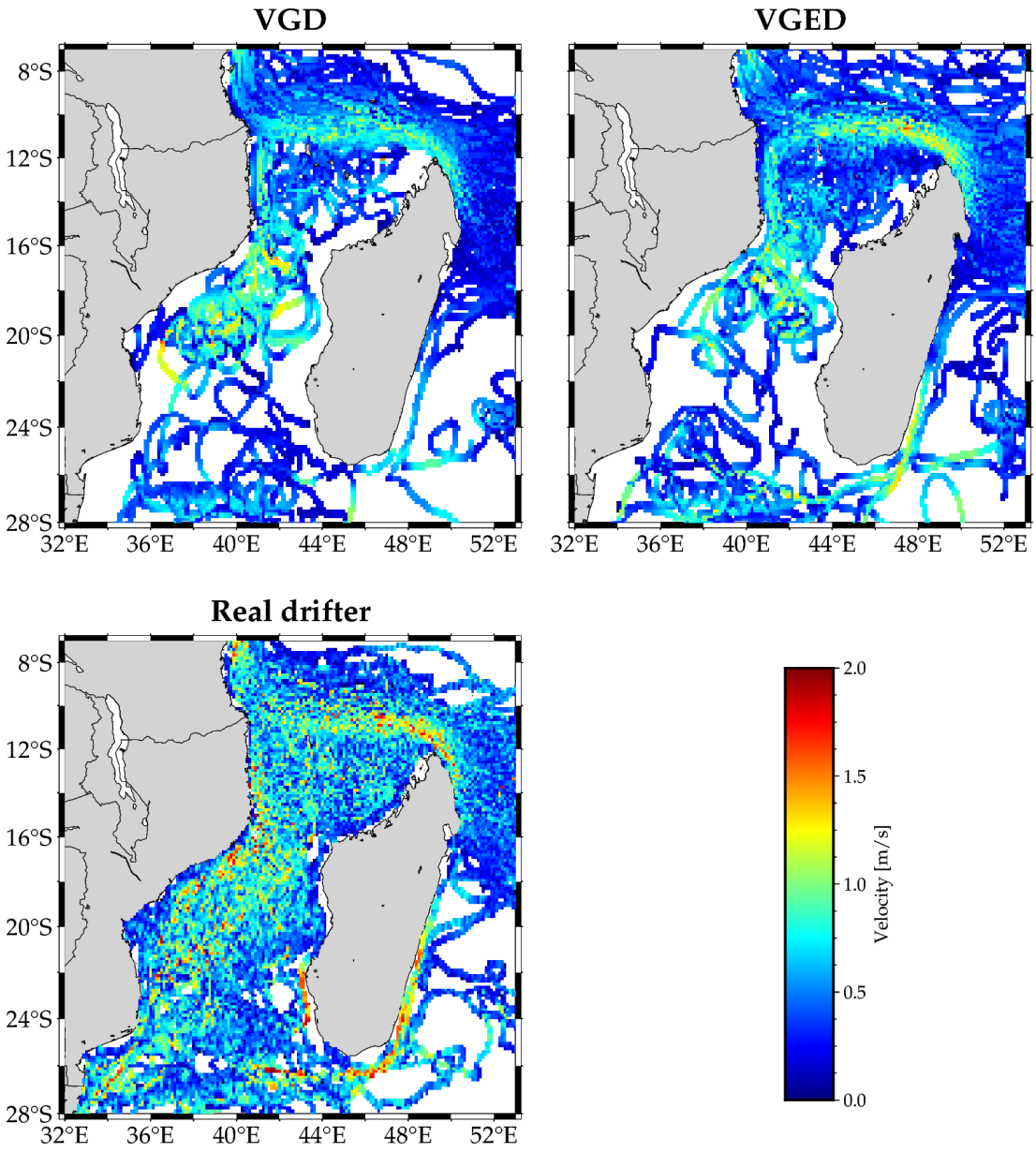

Figure 5.3: *Comparison of gridded $\frac{1}{8}^{\circ}$ mean velocities from 2000–2019, interpolated from all 151 real and virtual drifters. Blank areas represent regions without drifter data, where no velocity could be interpolated.*

The histograms (*Figure 5.4*) provide a detailed comparison of errors in position between real and virtual drifters, allowing for an assessment of how well the velocity fields replicate actual drifter positions simultaneously. Essentially, these plots show the difference in the position between real and virtual drifters at each time step.

One key observation was the concentration of position errors under 200 km for both velocity fields in EMC. This suggests that the geostrophic-only and geostrophic+Ekman currents, while not perfect, are reasonably effective in capturing the general movement of drifters within this error range. As the error distances increase, both velocity fields show a gradual decline in frequency. This means the concentration position error between real and virtual drifters was low or negligible after 400 km in EMC.

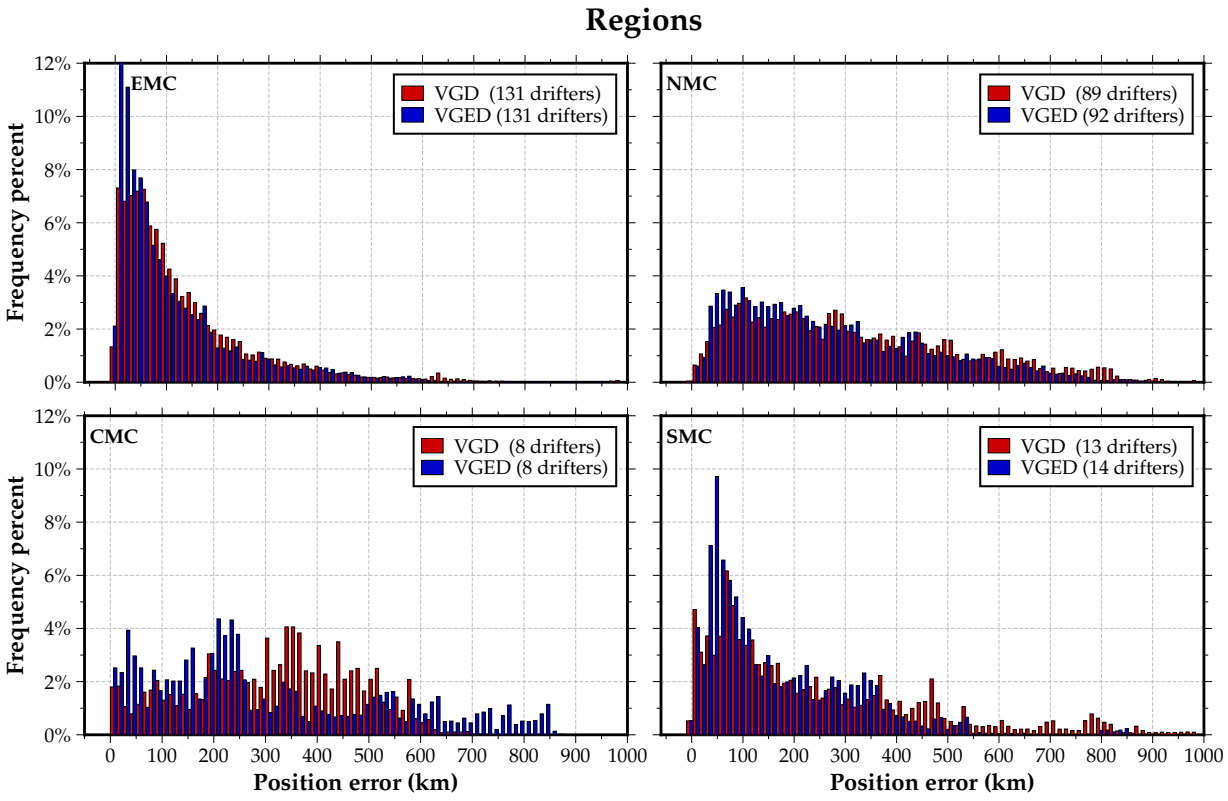

Figure 5.4: *Frequency distribution of error distances (in km) between real and virtual drifter for the Virtual Geostrophic Drifter (VGD) and Virtual Geostrophic-Ekman Drifter (VGED) across four regions of the domain (A: Eastern Madagascar Coast, B: Northern Mozambique Channel, C: Central Mozambique Channel, D: Southern Mozambique Channel). Error distances are shown as percentage frequencies with a bin width of 12.5km, comparing the performance of VGD (red) and VGD (blue) in replicating drifter trajectories. The frequency percentage in these histograms represents the relative occurrence of each position error across the dataset of drifters. Each bar in the histogram indicates the percentage of total measurements that fall within a particular range of position error.*

In the NMC, virtual drifters are still in high number, although there was a marginal difference between both virtual drifters. This difference was related to this region's wind component and these drifters' initial position. As seen in *Figure 3.1*, most of the drifters that travelled to NMC have an initial position in EMC. DiMarco et al.

(2002) also found that nearly all drifters that passed north of Cape Amber (north tip of Madagascar) continued westward between 10°S and 12°S toward the African coast. Because the VGD lacks a wind component, some of the VGD travel slowly enough and stay in the EMC, whereas VGED travels to NMC.

Although this histogram was right-skewed, the frequency was the lowest compared to the rest of the region. Another aspect was that the region registers high position errors. This results from a few virtual drifters being pushed further north of the African mainland coast by the bifurcation of the NEMC around 10°S (Voldsund et al., 2017). This means virtual drifters go south while real drifters go north, which propels high position errors.

In the CMC, although the frequency was marginally higher than NMC, this region has scattered position errors. High frequencies are not commonly seen in low position errors. This means the virtual drifter was, in fact, on a different path than the real drifter, especially the VGED. This highlights the region's complexity in simulating particle dispersion, characterised mostly by mesoscale eddies and specifically the linear and nonlinear ones (Halo & Raj, 2020). The region was so complex that Ridderinkhof and De Ruijter (2003) observed that seasonality does not affect the transport variability in this region.

The result from the reset of position for drifter 62575 in *Figure 5.1* and the original trajectory in *Figure 4.3* shows that the high concentration of position errors around 200 and 400 km could be linked to the scale of a typical eddy in this region (Backeberg et al., 2009).

One drifter difference in the SMC between virtual drifters was negligible, as some of these are advected from the south part of EMC. Few drifters passed through this region, showing a right-skewed histogram with low frequency compared to EMC, and VGD with extended tail of low frequency and high position error. Overall, VGED has a high frequency of around 50 km of position error and shows that Ekman dynamics was relevant in this region. The particularity of this region was that this receives drifters from CMC and south of EMC. Mostly, the eddies generated in the CMC travel southward and pass through this region. As discussed earlier, some drifters are caught in these moving eddies.

5.3 Drifter dispersion in Northern Offshore of Cabo Delgado

The deployment of virtual drifters within Area 4 offers meaningful perspectives into debris dispersion dynamics near Mozambique's major FLNG facility (*Figure 4.9*). Notably, the limited movement of VGED in winter indicate that Ekman dynamics play a crucial role. Winds in the NMC come from the south (Emílio, 2020), which clearly indicates why virtual drifters ran aground (represented by shorter distances). Assuming these south winds are stronger (Emílio, 2020), the Ekman drift was to the left of the direction of the wind, hence the short distance by those particles.

The differential performance between VGD and VGED underscores the impact of velocity fields on debris trajectories. VGED consistently ran aground along the Palma district in winter, highlighting the role of Ekman currents in directing debris movement, which was critical for risk assessment and mitigation strategies. VGD ability to traverse greater distances without immediate aground suggests a more resilient dispersal pattern under varying conditions.

These particles were run with geostrophic and Ekman currents, which are surface currents. Additional parameters should also be included to simulate the movement of debris in this region. Hart-Davis and Backeberg (2021) suggested that the particle trajectory model was most effective when accounting for wind, surface currents, and stochastic motion, as these factors accurately estimate the final position of the capsized vessel.

Another dataset by European Union-Copernicus Marine Service (2016) could be used as a velocity field for forecasting a 10-day debris dispersion if necessary for potential debris dispersion pathways, informing both environmental safeguards and emergency response frameworks for the FLNG operations. This dataset includes ageostrophic currents, such as waves and tidal drift, called SMOC (surface merged ocean current). This study did not analyse these ageostrophic currents, as they are mainly based on numerical models.

Chapter 6: CONCLUSION

The thesis aimed to develop a particle tracking model and Lagrangian parametrisations to characterise Mozambique Channel circulation using geostrophic-only and geostrophic+Ekman currents derived from CNES-CLS18 as the main velocity field. The model's parametrisation was designed to be simple and should be used in future works. This can describe current dynamics and be used for other processes, such as tracking ocean debris and larvae. The only caveat is finding an accurate representation of the real velocity field, which is a complex task.

The geostrophic-only and combined geostrophic and Ekman currents play a crucial role in determining the circulation in the Mozambique Channel. Upon thorough analysis, the following conclusion was reached:

- In the Eastern Madagascar Coast, the geostrophic-only currents showed the highest underestimation of velocities at 47%, which reduced to 22% with the inclusion of Ekman currents. Strong southward currents along this coast, influenced by wind-driven coastal upwelling, are well captured by VGED. Specific VGD in this region showed a strong contribution of formed dipole in the southern tip of Madagascar, which prevents movement of VGD to the Channel.
- In the Northern Mozambique Channel, underestimation was lower, at 18 and 20% for both geostrophic-only and combined geostrophic and Ekman, respectively. A western boundary current and seasonality characterise the region due to variability in the Northward East Madagascar Current and winds;
- In the Central Mozambique Channel, both velocity fields underestimated velocities by 18%. Although velocities are well represented, specific drifters showed that eddy linearity was responsible for high position error and virtual drifters moving out of eddies;
- In the Southern Mozambique Channel, underestimation was 33% with geostrophic currents, reduced to 24% when including Ekman dynamics. Moving eddies from the central Channel and southern tip of Madagascar greatly characterise this region. This region also features a mixture of linearity and nonlinearity in eddies, as cyclonic nonlinearity kept one of the lost drogue drifters following the eddy;
- Overall, the average underestimation across all regions was less than 30%, and the inclusion of Ekman drift showed a good representation of the circulation;
- Submesoscale structures, approximately 10 km in diameter, play a crucial role in biological production and influence the distribution of marine organisms. Unfortunately, none of the virtual drifters detected submesoscale processes, indicating resolution limitations;

- Ekman currents contribute significantly to surface circulation, especially during strong winds or atmospheric cyclones;
- The debris dispersion in Area 4 offshore of Cabo Delgado showed more significant variability with the geostrophic + Ekman velocity field constantly pushing debris ashore. This region, in general, was controlled by winds, and Ekman dynamics should be included when simulating future scenarios;
- The model can forecast currents accurately for five days when mesoscale eddies are present.

This study highlights the need for improved modelling approaches to accurately represent wind-driven dynamics in the Mozambique Channel. Enhanced observational data and higher-resolution velocity fields are essential for better understanding oceanic processes in this dynamic environment. Addressing these challenges will improve predictive capabilities for applications such as search and rescue operations, environmental safeguards and ecological studies.

Bibliography

Backeberg, B. C., Bertino, L., & Johannessen, J. A. (2009). Evaluating two numerical advection schemes in HYCOM for eddy-resolving modelling of the Agulhas Current. *Ocean Science*, *5*(2), 173–190. https://doi.org/10.5194/os-5-173-2009

Backeberg, B. C., Johannessen, J. A., Bertino, L., & Reason, C. J. (2008). The greater Agulhas Current system: An integrated study of its mesoscale variability. *Journal of Operational Oceanography*, *1*(1), 29–44. https://doi.org/10.1080/1755876X.2008.11020093

Backeberg, B. C., & Reason, C. J. C. (2010). A connection between the South Equatorial Current north of Madagascar and Mozambique Channel Eddies. *Geophysical Research Letters*, *37*(4), 2009GL041950. https://doi.org/10.1029/2009GL041950

Backeberg, B. C., Counillon, F., Johannessen, J. A., & Pujol, M.-.-I. (2014). Assimilating along-track SLA data using the EnOI in an eddy resolving model of the Agulhas system. *Ocean Dynamics*, *64*(8), 1121–1136. https://doi.org/10.1007/s10236-014-0717-6

Chelton, D. B., Gaube, P., Schlax, M. G., Early, J. J., & Samelson, R. M. (2011). The Influence of Nonlinear Mesoscale Eddies on Near-Surface Oceanic Chlorophyll. *Science*, *334*(6054), 328–332. https://doi.org/10.1126/science.1208897

Constantin, A., & Johnson, R. (2018). Steady Large-Scale Ocean Flows in Spherical Coordinates. *Oceanography*, *31*(3), 42–50. https://doi.org/10.5670/oceanog.2018.308

Cossa, O., Pous, S., Penven, P., Capet, X., & Reason, C. (2016). Modelling cyclonic eddies in the Delagoa Bight region. *Continental Shelf Research*, *119*, 14–29. https://doi.org/10.1016/j.csr.2016.03.006

De Ruijter, W. P. M., Ridderinkhof, H., Lutjeharms, J. R. E., Schouten, M. W., & Veth, C. (2002). Observations of the flow in the Mozambique Channel. *Geophysical Research Letters*, *29*(10). https://doi.org/10.1029/2001GL013714

DiMarco, S. F., Chapman, P., Nowlin, W. D., Hacker, P., Donohue, K., Luther, M., Johnson, G. C., & Toole, J. (2002). Volume transport and property distributions of the Mozambique Channel. *Deep Sea Research Part II: Topical Studies in Oceanography*, *49*(7-8), 1481–1511. https://doi.org/10.1016/S0967-0645(01)00159-X

Donguy, J., & Meyers, G. (1995). Observations of geostrophic transport variability in the western tropical Indian Ocean. *Deep Sea Research Part I: Oceanographic Research Papers*, *42*(6), 1007–1028. https://doi.org/10.1016/0967-0637(95)00047-A

Ekman, V. W. (1905). On the influence of the earth's rotation on ocean-currents.

Elipot, S., Lumpkin, R., Perez, R. C., Lilly, J. M., Early, J. J., & Sykulski, A. M. (2016). A global surface drifter data set at hourly resolution. *Journal of Geophysical Research: Oceans*, *121*(5), 2937–2966. https://doi.org/10.1002/2016JC011716

Elipot, S., Sykulski, A., Lumpkin, R., Centurioni, L., & Pazos, M. (2022a). Hourly location, current velocity, and temperature collected from Global Drifter Program drifters world-wide. https://doi.org/10.25921/X46C-3620

Elipot, S., Sykulski, A., Lumpkin, R., Centurioni, L., & Pazos, M. (2022b). A dataset of hourly sea surface temperature from drifting buoys. *Scientific Data*, *9*(1), 567. https://doi.org/10.1038/s41597-022-01670-2

Emílio, C. A. (2020). *Campos de Vento e Circulação oceânica no Canal de Moçambique: perspectivas a partir de diferentes estimativas* [Dissertação de Mestrado em Oceanografia Aplicada]. Universidade Eduardo Mondlane.

European Union-Copernicus Marine Service. (2016). Global Ocean 1/12° Physics Analysis and Forecast updated Daily. https://doi.org/10.48670/MOI-00016

European Union-Copernicus Marine Service. (2021). GLOBAL OCEAN ALONG-TRACK L3 SEA SURFACE HEIGHTS REPROCESSED (1993-ONGOING) TAILORED FOR DATA ASSIMILATION. https://doi.org/10.48670/MOI-00146

European Union-Copernicus Marine Service. (2023). Global Total (copernicus-Globcurrent), Ekman and Geostrophic Currents at the Surface and 15m. https://doi.org/10.48670/MDS-00327

GDP. (n.d.). List and details of all buoys in database as of December 31, 2023 (Created on: Thu Mar 21 12:57:02 EDT 2024).

Gerdan, G. P., & Deakin, R. E. (1999). Transforming cartesian coordinates *X, Y, Z* to geographical coordinates ϕ, λ, *h*. *Australian Surveyor*, *44*(1), 55–63. https://doi.org/10.1080/00050326.1999.10441904

Gründlingh, M. L. (1987). Cyclogenesis in the mozambique ridge current. *Deep Sea Research Part A. Oceanographic Research Papers*, *34*(1), 89–103. https://doi.org/10.1016/0198-0149(87)90124-5

Gründlingh, M. L. (1989). Two contra-rotating eddies of the Mozambique Ridge Current. *Deep Sea Research Part A. Oceanographic Research Papers*, *36*(1), 149–153. https://doi.org/10.1016/0198-0149(89)90024-1

Gründlingh, M. L. (1993). On the winter flow in the southern Mozambique channel. *Deep Sea Research Part I: Oceanographic Research Papers*, *40*(2), 409–418. https://doi.org/10.1016/0967-0637(93)90011-Q

Halo, I., Backeberg, B., Penven, P., Ansorge, I., Reason, C., & Ullgren, J. (2014). Eddy properties in the Mozambique Channel: A comparison between observations and two numerical ocean circulation models. *Deep Sea Research Part II: Topical Studies in Oceanography*, *100*, 38–53. https://doi.org/10.1016/j.dsr2.2013.10.015

Halo, I., & Raj, R. P. (2020). Comparative oceanographic eddy variability during climate change in the Agulhas Current and Somali Coastal Current Large Marine Ecosystems. *Environmental Development*, *36*, 100586. https://doi.org/10.1016/j.envdev.2020.100586

Hancke, L., Roberts, M., & Ternon, J. (2014). Surface drifter trajectories highlight flow pathways in the Mozambique Channel. *Deep Sea Research Part II: Topical Studies in Oceanography*, *100*, 27–37. https://doi.org/10.1016/j.dsr2.2013.10.014

Harlander, U., Ridderinkhof, H., Schouten, M. W., & De Ruijter, W. P. M. (2009). Long-term observations of transport, eddies, and Rossby waves in the Mozambique Channel. *Journal of Geophysical Research: Oceans*, *114*(C2), 2008JC004846. https://doi.org/10.1029/2008JC004846

Harris, T. (1972). Sources of the Agulhas current in the spring of 1964. *Deep Sea Research and Oceanographic Abstracts*, *19*(9), 633–650. https://doi.org/10.1016/0011-7471(72)90091-5

Hart-Davis, M. G., & Backeberg, B. C. (2021). Towards a particle trajectory modelling approach in support of South African search and rescue operations at sea. *Journal of Operational Oceanography*, 1–9. https://doi.org/10.1080/1755876X.2021.1911485

Hart-Davis, M. G., Backeberg, B. C., Halo, I., van Sebille, E., & Johannessen, J. A. (2018). Assessing the accuracy of satellite derived ocean currents by comparing observed and virtual buoys in the Greater Agulhas Region. *Remote Sensing of Environment*, *216*, 735–746. https://doi.org/10.1016/j.rse.2018.03.040

Langa, A. A. A., & Calil, P. H. R. (2020). On the role of physical processes on the surface chlorophyll variability in the Northern Mozambique Channel. *Ocean Dynamics*, *70*(1), 95–114. https://doi.org/10.1007/s10236-019-01311-0

Lange, M., & van Sebille, E. (2017). Parcels v0.9: Prototyping a Lagrangian ocean analysis framework for the petascale age. *Geoscientific Model Development*, *10*(11), 4175–4186. https://doi.org/10.5194/gmd-10-4175-2017

Lumpkin, R., Özgökmen, T., & Centurioni, L. (2017). Advances in the Application of Surface Drifters. *Annual Review of Marine Science*, *9*(1), 59–81. https://doi.org/10.1146/annurev-marine-010816-060641

Lumpkin, R., & Pazos, M. (2007, May). Measuring surface currents with Surface Velocity Program drifters: The instrument, its data, and some recent results. In A. Griffa, A. D. Kirwan Jr., A. J. Mariano, T. Özgökmen & H. T. Rossby (Eds.), *Lagrangian Analysis and Prediction of Coastal and Ocean Dynamics* (1st ed., pp. 39–67). Cambridge University Press. https://doi.org/10.1017/CBO9780511535901.003

Lutjeharms, J. R., Biastoch, A., Van Der Werf, P. M., Ridderinkhof, H., & De Ruijter, W. P. (2012). On the discontinuous nature of the Mozambique Current. *South African Journal of Science*, *108*(1/2), 5 pages. https://doi.org/10.4102/sajs.v108i1/2.428

Ma, Y., Weldeab, S., Schneider, R. R., Andersen, N., Garbe-Schönberg, D., & Friedrich, T. (2021). Strong Southern African Monsoon and weak Mozambique Channel throughflow during Heinrich events: Implica-

tion for Agulhas leakage. *Earth and Planetary Science Letters*, *574*, 117148. https://doi.org/10.1016/j.epsl.2021.117148

Malauene, B., Shillington, F., Roberts, M., & Moloney, C. (2014). Cool, elevated chlorophyll-a waters off northern Mozambique. *Deep Sea Research Part II: Topical Studies in Oceanography*, *100*, 68–78. https://doi.org/10.1016/j.dsr2.2013.10.017

Menna, M., Poulain, P.-M., Bussani, A., & Gerin, R. (2018). Detecting the drogue presence of SVP drifters from wind slippage in the Mediterranean Sea. *Measurement*, *125*, 447–453. https://doi.org/10.1016/j.measurement.2018.05.022

Mulet, S., Rio, M.-H., Etienne, H., Artana, C., Cancet, M., Dibarboure, G., Feng, H., Husson, R., Picot, N., Provost, C., & Strub, P. T. (2021). The new CNES-CLS18 global mean dynamic topography. *Ocean Science*, *17*(3), 789–808. https://doi.org/10.5194/os-17-789-2021

Niiler, P. (2001). Chapter 4.1 The world ocean surface circulation. In *International Geophysics* (pp. 193–204, Vol. 77). Elsevier. https://doi.org/10.1016/S0074-6142(01)80119-4

Noor, N. M., Al Bakri Abdullah, M. M., Yahaya, A. S., & Ramli, N. A. (2014). Comparison of Linear Interpolation Method and Mean Method to Replace the Missing Values in Environmental Data Set. *Materials Science Forum*, *803*, 278–281. https://doi.org/10.4028/www.scientific.net/MSF.803.278

Onink, V., Wichmann, D., Delandmeter, P., & Sebille, E. (2019). The Role of Ekman Currents, Geostrophy, and Stokes Drift in the Accumulation of Floating Microplastic. *Journal of Geophysical Research: Oceans*, *124*(3), 1474–1490. https://doi.org/10.1029/2018JC014547

Pond, S., & Pickard, G. L. (1983). *Introductory Dynamical Oceanography* (2nd). Elsevier. https://doi.org/10.1016/C2009-0-24288-7

Pujol, M.-I., Faugère, Y., Taburet, G., Dupuy, S., Pelloquin, C., Ablain, M., & Picot, N. (2016). DUACS DT2014: The new multi-mission altimeter data set reprocessed over 20years. *Ocean Science*, *12*(5), 1067–1090. https://doi.org/10.5194/os-12-1067-2016

Ridderinkhof & De Ruijter, W. (2003). Moored current observations in the Mozambique Channel. *Deep Sea Research Part II: Topical Studies in Oceanography*, *50*(12-13), 1933–1955. https://doi.org/10.1016/S0967-0645(03)00041-9

Ridderinkhof, Le Bars, D., Von Der Heydt, A. S., & De Ruijter, W. P. M. (2013). Dipoles of the South East Madagascar Current. *Geophysical Research Letters*, *40*(3), 558–562. https://doi.org/10.1002/grl.50157

Rio, M.-H., Mulet, S., & Picot, N. (2014). Beyond GOCE for the ocean circulation estimate: Synergetic use of altimetry, gravimetry, and in situ data provides new insight into geostrophic and Ekman currents: Ocean circulation beyond GOCE. *Geophysical Research Letters*, *41*(24), 8918–8925. https://doi.org/10.1002/2014GL061773

Roberts, M. J., Ternon, J.-F., & Morris, T. (2014). Interaction of dipole eddies with the western continental slope of the Mozambique Channel. *Deep Sea Research Part II: Topical Studies in Oceanography*, *100*, 54–67. https://doi.org/10.1016/j.dsr2.2013.10.016

Sætre, R. (1985). Surface currents in the Mozambique channel. *Deep Sea Research Part A. Oceanographic Research Papers*, *32*(12), 1457–1467. https://doi.org/10.1016/0198-0149(85)90097-4

Sætre, R., & Da Silva, A. J. (1984). The circulation of the Mozambique channel. *Deep Sea Research Part A. Oceanographic Research Papers*, *31*(5), 485–508. https://doi.org/10.1016/0198-0149(84)90098-0

Said, M., El-Gindy, A., & Radwan, A. (2013). Surface Circulation of the Egyptian Mediterranean Waters Using Satellite-Tracked Lagrangian Drifters. *Journal of King Abdulaziz University-Marine Sciences*, *24*(1), 69–81. https://doi.org/10.4197/Mar.24-1.6

Schouten, M. W., De Ruijter, W. P. M., Van Leeuwen, P. J., & Dijkstra, H. A. (2002a). An oceanic teleconnection between the equatorial and southern Indian Ocean. *Geophysical Research Letters*, *29*(16). https://doi.org/10.1029/2001GL014542

Schouten, M. W., De Ruijter, W. P. M., & Van Leeuwen, P. J. (2002b). Upstream control of Agulhas Ring shedding. *Journal of Geophysical Research: Oceans*, *107*(C8). https://doi.org/10.1029/2001JC000804

Schouten, M. W., De Ruijter, W. P., Van Leeuwen, P. J., & Ridderinkhof, H. (2003). Eddies and variability in the Mozambique Channel. *Deep Sea Research Part II: Topical Studies in Oceanography*, *50*(12-13), 1987–2003. https://doi.org/10.1016/S0967-0645(03)00042-0

Stewart, R. H. (2008, September). *Introduction To Physical Oceanography*. Texas A & M University.

Swart, N. C., Lutjeharms, J. R. E., Ridderinkhof, H., & De Ruijter, W. P. M. (2010). Observed characteristics of Mozambique Channel eddies. *Journal of Geophysical Research: Oceans*, *115*(C9), 2009JC005875. https://doi.org/10.1029/2009JC005875

Talley, L. D., Pickard, G. L., Emery, W. J., & Swift, J. H. (Eds.). (2011). *Descriptive physical oceanography: An introduction* (6. ed). Elsevier, AP.

Ternon, J., Bach, P., Barlow, R., Huggett, J., Jaquemet, S., Marsac, F., Ménard, F., Penven, P., Potier, M., & Roberts, M. (2014a). The Mozambique Channel: From physics to upper trophic levels. *Deep Sea Research Part II: Topical Studies in Oceanography*, *100*, 1–9. https://doi.org/10.1016/j.dsr2.2013.10.012

Ternon, J., Roberts, M., Morris, T., Hancke, L., & Backeberg, B. (2014b). In situ measured current structures of the eddy field in the Mozambique Channel. *Deep Sea Research Part II: Topical Studies in Oceanography*, *100*, 10–26. https://doi.org/10.1016/j.dsr2.2013.10.013

Tew-Kai, E., & Marsac, F. (2009). Patterns of variability of sea surface chlorophyll in the Mozambique Channel: A quantitative approach. *Journal of Marine Systems*, *77*(1-2), 77–88. https://doi.org/10.1016/j.jmarsys.2008.11.007

Tian, D., Uieda, L., Leong, W. J., Fröhlich, Y., Schlitzer, W., Grund, M., Jones, M., Toney, L., Yao, J., Magen, Y., Jing-Hui, T., Materna, K., Belem, A., Newton, T., Anant, A., Ziebarth, M., Quinn, J., & Wessel, P. (2024, May). PyGMT: A Python interface for the Generic Mapping Tools. https://doi.org/10.5281/ZENODO.3781524

Tomczak, M., & Godfrey, J. S. (1994). *Regional Oceanography: An Introduction*. Elsevier. https://doi.org/10.1016/C2009-0-14825-0

Ullgren, J. E., André, E., Gammelsrød, T., & Hoguane, A. M. (2016). Observations of strong ocean current events offshore Pemba, Northern Mozambique. *Journal of Operational Oceanography*, *9*(1), 55–66. https://doi.org/10.1080/1755876X.2016.1204172

Ullgren, J. E., Van Aken, H., Ridderinkhof, H., & De Ruijter, W. (2012). The hydrography of the Mozambique Channel from six years of continuous temperature, salinity, and velocity observations. *Deep Sea Research Part I: Oceanographic Research Papers*, *69*, 36–50. https://doi.org/10.1016/j.dsr.2012.07.003

Vianello, P., Herbette, S., Ternon, J.-F., Demarcq, H., & Roberts, M. J. (2020). Observation of a mesoscale eddy dipole on the northern Madagascar Ridge: Consequences for the circulation and hydrography in the vicinity of a seamount. *Deep Sea Research Part II: Topical Studies in Oceanography*, *176*, 104815. https://doi.org/10.1016/j.dsr2.2020.104815

Vinayachandran, P. N. M., Masumoto, Y., Roberts, M. J., Huggett, J. A., Halo, I., Chatterjee, A., Amol, P., Gupta, G. V. M., Singh, A., Mukherjee, A., Prakash, S., Beckley, L. E., Raes, E. J., & Hood, R. (2021). Reviews and syntheses: Physical and biogeochemical processes associated with upwelling in the Indian Ocean. *Biogeosciences*, *18*(22), 5967–6029. https://doi.org/10.5194/bg-18-5967-2021

Voldsund, A., Aguiar-González, B., Gammelsrød, T., Krakstad, J.-O., & Ullgren, J. (2017). Observations of the East Madagascar Current system: Dynamics and volume transports. *Journal of Marine Research*, *75*(4), 531–555. https://doi.org/10.1357/002224017821836725

Zheng, S., Du, Y., Li, J., & Cheng, X. (2015). Eddy characteristics in the South Indian Ocean as inferred from surface drifters. *Ocean Science*, *11*(3), 361–371. https://doi.org/10.5194/os-11-361-2015

Appendix A: Method Description

A.1 Cartesian coordinates from geographical coordinates

The equations presented in this section describe the transformation from geographical coordinates to Cartesian coordinates. *Equation A.1* calculates the squared eccentricity e^2 of the Earth's ellipsoid using the semi-major axis a and semi-minor axis b, which quantifies the ellipsoid's deviation from a perfect sphere. *Equation A.2* determines the radius of curvature in the prime vertical ν at a given latitude ϕ, essential for accurate projection. Finally, *Equation A.3* converts the geographical coordinates—latitude ϕ, longitude λ, and altitude to three-dimensional Cartesian coordinates (x, y, z). These equations were adapted from Gerdan and Deakin (1999).

$$e^2 = \frac{a^2 - b^2}{a^2}, \tag{A.1}$$

$$\nu = \frac{a}{\sqrt{1 - e^2 \cdot \sin^2(\phi)}}, \tag{A.2}$$

$$\begin{cases} x = (\nu + \text{alt}) \cdot \cos(\phi) \cdot \cos(\lambda) \\ y = (\nu + \text{alt}) \cdot \cos(\phi) \cdot \sin(\lambda) \\ z = [(1 - e^2) \cdot \nu + \text{alt}] \cdot \sin(\phi) \end{cases} \tag{A.3}$$

A.2 Geographical coordinates from cartesian coordinates

These equations describe the transformation from Cartesian coordinates to geographical coordinates. *Equation A.4* calculates the second eccentricity squared e'^2 of the Earth's ellipsoid using the semi-major axis a and semi-minor axis b, which accounts for the ellipsoid's shape. *Equation A.5* computes the projection p from the Cartesian coordinates (x, y), representing the distance from the Earth's axis. *Equation A.6* determines an initial estimate of the latitude ϕ_0 using the Cartesian coordinates (x, y, z) and the second eccentricity. Finally, *Equation A.7* refines the latitude ϕ by incorporating the radius of curvature ν and the previously calculated ϕ_0. It also calculates the longitude λ from the Cartesian coordinates x and y. These equations were adapted from Gerdan and Deakin (1999).

$$e'^2 = \frac{a^2 - b^2}{b^2} \tag{A.4}$$

$$p = \sqrt{x^2 + y^2} \tag{A.5}$$

$$\tan(\phi_0) = \frac{z \cdot (1 + e'^2)}{p} \tag{A.6}$$

$$\begin{cases} \tan(\phi) = \dfrac{z + \nu \cdot e^2 \cdot \sin(\phi_0)}{p} \\ \\ \tan(\lambda) = \dfrac{y}{x} \end{cases} \tag{A.7}$$

Appendix B: Global Drifter Program

Table B.1: *GDP drifters characteristics IDs.*

Drifter type	Years	IDs	Details
SVP	2000, 2001, 2003, 2004, 2005, 2006, 2007, 2008, 2009, 2010, 2013, 2015, 2017, 2018, 2019	17442, 27629, 34381, 34376, 34212, 24054, 34396, 45955, 45957, 45978, 45937, 2444344, 54374, 2444348, 2339263, 2444347, 52948, 52950, 44131, 62281, 45963, 44055, 44646, 71201, 75252, 90510, 90507, 114830, 114824, 114803, 114579, 114811, 114571, 114826, 109582, 109587, 139777, 139775, 139776, 64826320, 64827010, 145732, 64827410, 145724, 63945570, 145779, 66712370	(GDP, n.d.) | Link
SVPB	2001, 2002, 2003, 2004, 2005, 2006, 2007, 2008, 2009, 2010, 2011, 2012, 2013, 2014, 2015, 2016, 2017, 2018, 2019	2931, 18688, 32939, 35467, 30723, 2340549, 34160, 2134164, 46026, 46027, 2344299, 24828, 52954, 53421, 53415, 57899, 57894, 63905, 63908, 40553, 41298, 40549, 40551, 40556, 70958, 36163, 63896, 63895, 70960, 34176, 83506, 46070, 34178, 62575, 49509, 70972, 71016, 70946, 97854, 41534, 10308830, 88672, 88655, 38554, 10409000, 79586, 113732, 71033, 101939, 109365, 109378, 109382, 109380, 109374, 109379, 109372, 109291, 38628, 101583, 109549, 101590, 101580, 101702, 101814, 101665, 126952, 101714, 60650200, 109361, 126946, 101656, 101833, 101668, 126945, 127053, 60751210, 127055, 109547, 60751580, 127056, 60751420, 133658, 133651, 127051, 132528, 116049, 101670, 132681, 63041010, 63042070, 60751430, 63896920, 63471560, 129290, 63470540, 63998730, 63996880, 62443600, 64803190, 66511990, 67209520, 63568430, 65804070	(GDP, n.d.) | Link
SVPBW	2002	28699	(GDP, n.d.) | Link

Appendix C: Tropical Cyclones

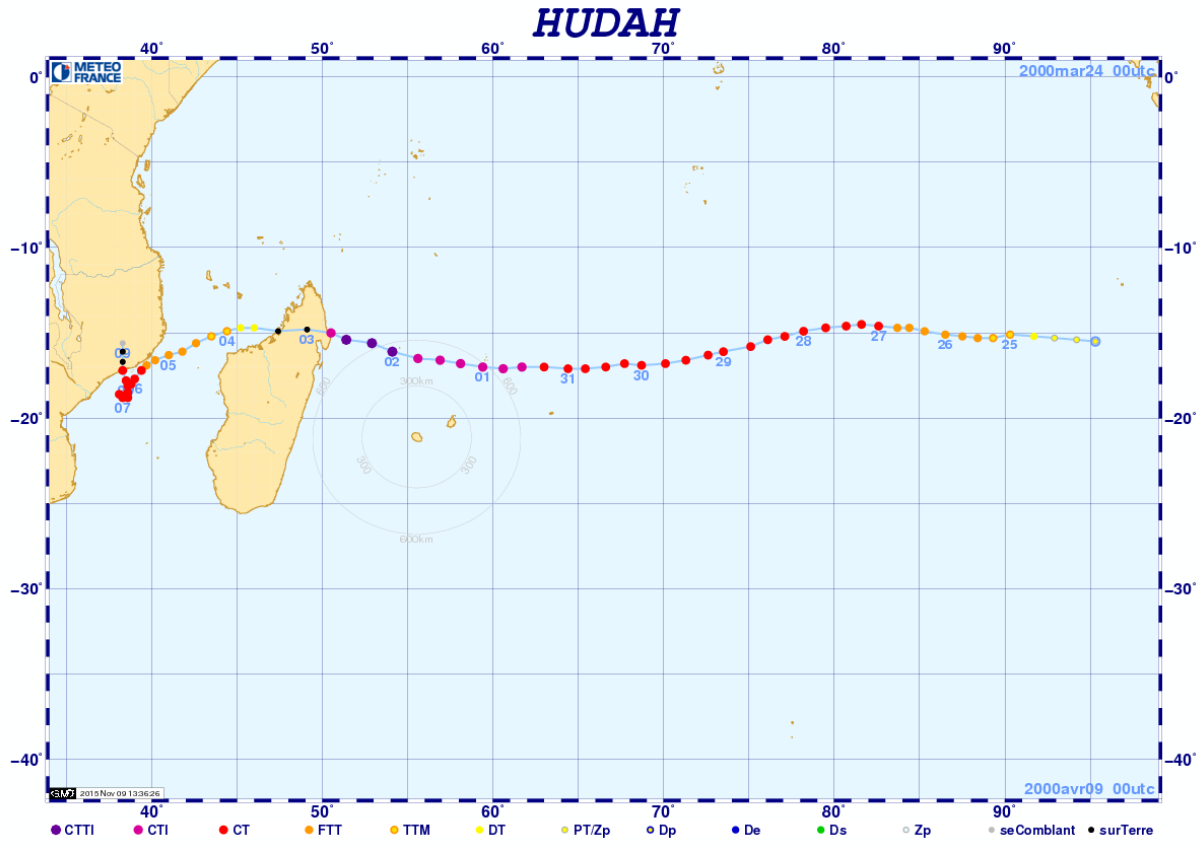

Figure C.1: *Track of Tropical Cyclone Hudah in the Southwest Indian Ocean, showing its progression from March 24, 2000, to April 9, 2000. The coloured dots represent different stages of intensity, following the standard classification system: CTTI (Cyclonic Tropical Storm), CTI (Intense Tropical Cyclone), CT (Tropical Cyclone), FTT (Moderate Tropical Storm), and TTM (Tropical Depression), with each stage depicted along the track based on meteorological data. Image from Météo France archives.*

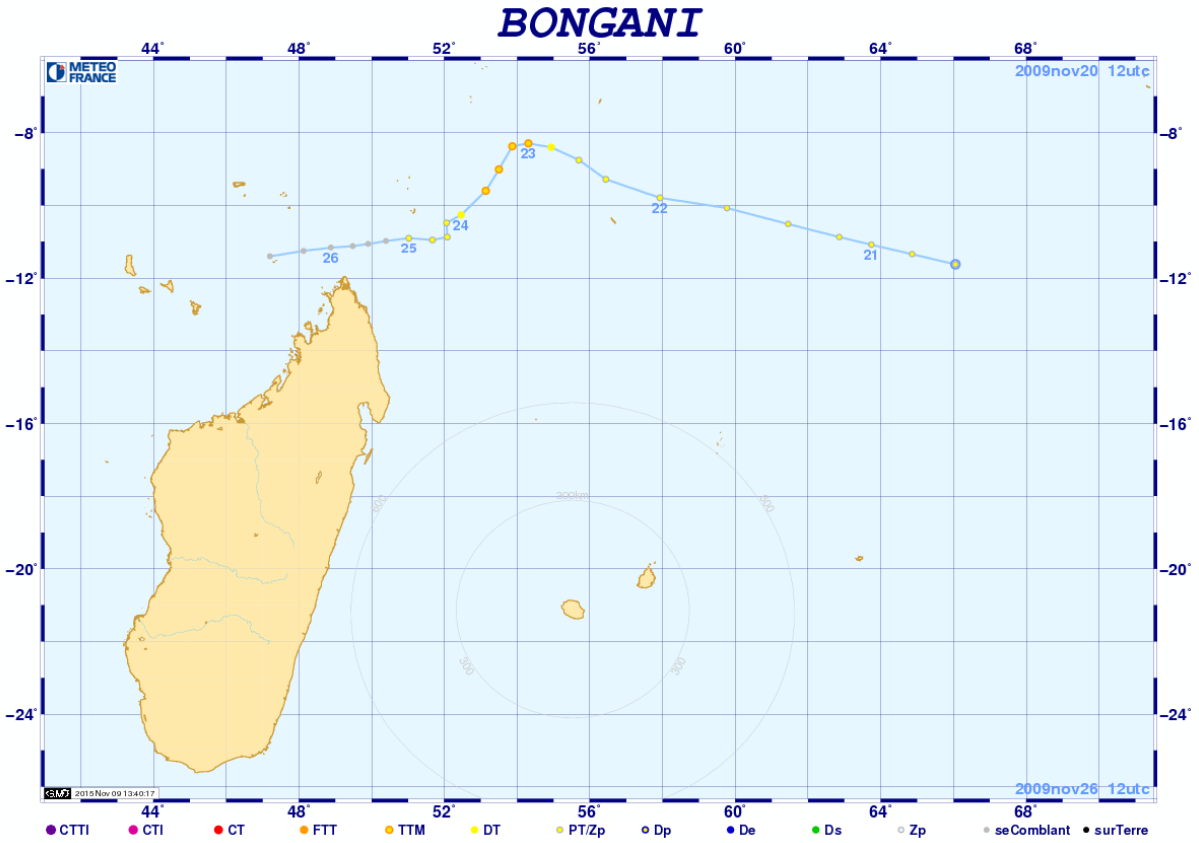

Figure C.2: *Track of Moderate Tropical Storm Bongani in the Southwest Indian Ocean, depicting its trajectory from November 20, 2009, to November 26, 2009. The cyclone moved north of Madagascar and gradually weakened. The coloured dots along the path indicate the cyclone's intensity stages: CTTI (Cyclonic Tropical Storm), CTI (Intense Tropical Cyclone), CT (Tropical Cyclone), FTT (Moderate Tropical Storm), TTM (Tropical Depression), and DT (Tropical Disturbance). Image from Météo France archives.*

Appendix D: Virtual drifter dispersion within offshore of Cabo Delgado

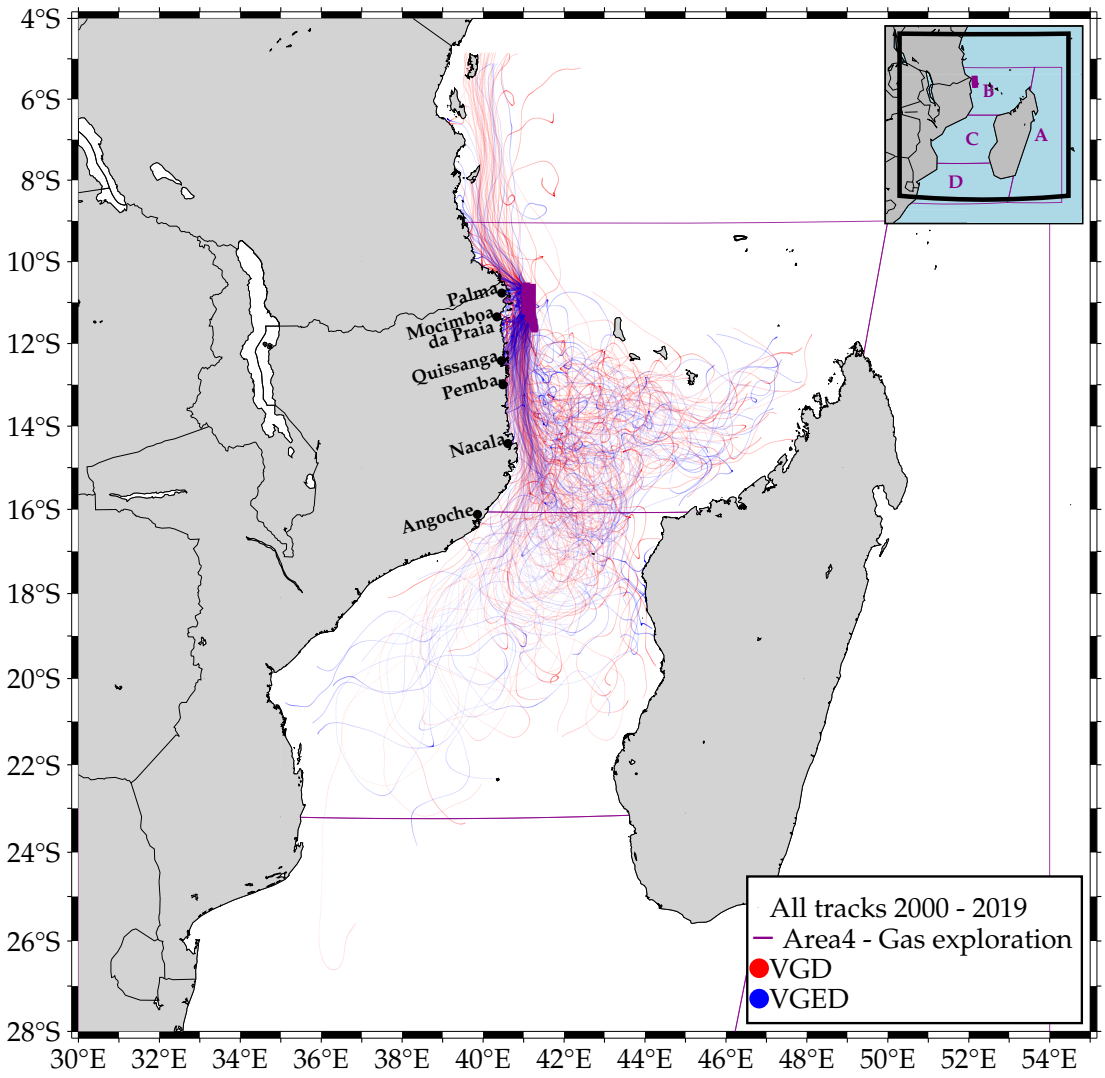

Figure D.1: *Trajectories of 480 virtual drifters, with half for VGD and half for VGED. These were released inside Area 4 (represented with magenta) of FLNG facility on the offshore coast of Cabo Delgado. The trajectories were calculated using the Geostrophic-only velocity field, represented in red, and the Geostrophic+Ekman velocity field, represented in blue. The figure represents an overlap of trajectories from 2000 to 2019.*